Geochemistry, Geophysics, Geosystems

RESEARCH ARTICLE
10.1029/2020GC009095

# Focused Fluid Flow Along the Nootka Fault Zone and Continental Slope, Explorer-Juan de Fuca Plate Boundary

**M. Riedel[1], K. M. M. Rohr[2], G. D. Spence[3], D. Kelley[4], J. Delaney[4], L. Lapham[5], J. W. Pohlman[6], R. D. Hyndman[2,3], and E. C. Willoughby[7]**

[1]GEOMAR Helmholtz Centre for Ocean Research Kiel, Kiel, Germany, [2]Geological Survey of Canada – Pacific, Sidney, British Columbia, Canada, [3]School of Earth and Ocean Sciences, University of Victoria, Victoria, British Columbia, Canada, [4]School of Oceanography, University of Washington, Seattle, WA, USA, [5]Centre for Environmental Science, Chesapeake Biological Laboratory, University of Maryland, Solomons, MD, USA, [6]Woods Hole Coastal and Marine Science Center, U.S. Geological Survey, Woods Hole, MA, USA, [7]Ronin Institute, Montclair, NJ, USA

**Key Points:**
- Fluid flow is focused along Nootka Fault traces resulting in shallow bright spots
- Two seafloor mounds are the result of basaltic intrusions in the Nootka fault zone
- Gas hydrates occur at the Nootka Slope and are imaged seismically as bottom-simulating reflectors suggesting a regional heat flow of ~80 mW/m$^2$ along the slope

**Supporting Information:**
- Supporting Information S1

**Correspondence to:**
M. Riedel,
mriedel@geomar.de

**Citation:**
Riedel, M., Rohr, K. M. M., Spence, G. D., Kelley, D., Delaney, J., Lapham, L., et al. (2020). Focused fluid flow along the Nootka fault zone and continental slope, Explorer-Juan de Fuca plate boundary. *Geochemistry, Geophysics, Geosystems*, *21*, e2020GC009095. https://doi.org/10.1029/2020GC009095

Received 16 APR 2020
Accepted 31 JUL 2020
Accepted article online 7 AUG 2020



**Abstract** Geophysical and geochemical data indicate there is abundant fluid expulsion in the Nootka fault zone (NFZ) between the Juan de Fuca and Explorer plates and the Nootka continental slope. Here we combine observations from >20 years of investigations to demonstrate the nature of fluid-flow along the NFZ, which is the seismically most active region off Vancouver Island. Seismicity reaching down to the upper mantle is linked to near-seafloor manifestation of fluid flow through a network of faults. Along the two main fault traces, seismic reflection data imaged bright spots 100–300 m below seafloor that lie above changes in basement topography. The bright spots are conformable to sediment layering, show opposite-to-seafloor reflection polarity, and are associated with frequency reduction and velocity push-down indicating the presence of gas in the sediments. Two seafloor mounds ~15 km seaward of the Nootka slope are underlain by deep, nonconformable high-amplitude reflective zones. Measurements in the water column above one mound revealed a plume of warm water, and bottom-video observations imaged hydrothermal vent system biota. Pore fluids from a core at this mound contain predominately microbial methane ($C_1$) with a high proportion of ethane ($C_2$) yielding $C_1/C_2$ ratios <500 indicating a possible slight contribution from a deep source. We infer the reflective zones beneath the two mounds are basaltic intrusions that create hydrothermal circulation within the overlying sediments. Across the Nootka continental slope, gas hydrate-related bottom-simulating reflectors are widespread and occur at depths indicating heat flow values of 80–90 mW/m$^2$.

## 1. Introduction

The Cascadia subduction zone stretching from northern Vancouver Island to Cape Mendocino in northern California is characterized by the mainly oblique subduction of the Juan de Fuca plate system beneath the North American plate. To the north, the Juan de Fuca plate system is fragmented into the Explorer plate and the Winona Basin (Figure 1), each with significant internal deformation. The Nootka transform fault is the boundary between the Juan de Fuca and the Explorer Plates off central Vancouver Island with a ridge-fault-fault triple junction at its western end in Middle Valley and a fault trench-trench triple junction at its eastern end on the Vancouver Island margin. The fault has been described previously in some detail (e.g., Cassidy et al., 1998; Hyndman et al., 1979; Rohr et al., 2018). It was identified from seismic reflection data as a 20 km-wide zone of intense faulting and seismicity associated with left-lateral strike-slip motion at 2–3 cm/year (Hyndman et al., 1979). The fault is the major source of seismicity off Vancouver Island, with a few historical earthquake magnitudes up to Mw 6.6 (Braunmiller & Nábělek, 2002; Hutchinson et al., 2019; Ristau et al., 2006), and thus represents a significant geohazard to coastal British Columbia. The northern end of the fault zone on the abyssal plane is, however, dominated by high rates of microseismicity (Hutchinson et al., 2019; Figure 2a). Two subparallel seismicity lineations in the north and south delineate the Nootka fault zone (NFZ) (Hutchinson et al., 2019), as defined previously from seismic reflection imaging by Hyndman et al. (1979) and later refined by including multibeam data (Rohr et al., 2018).

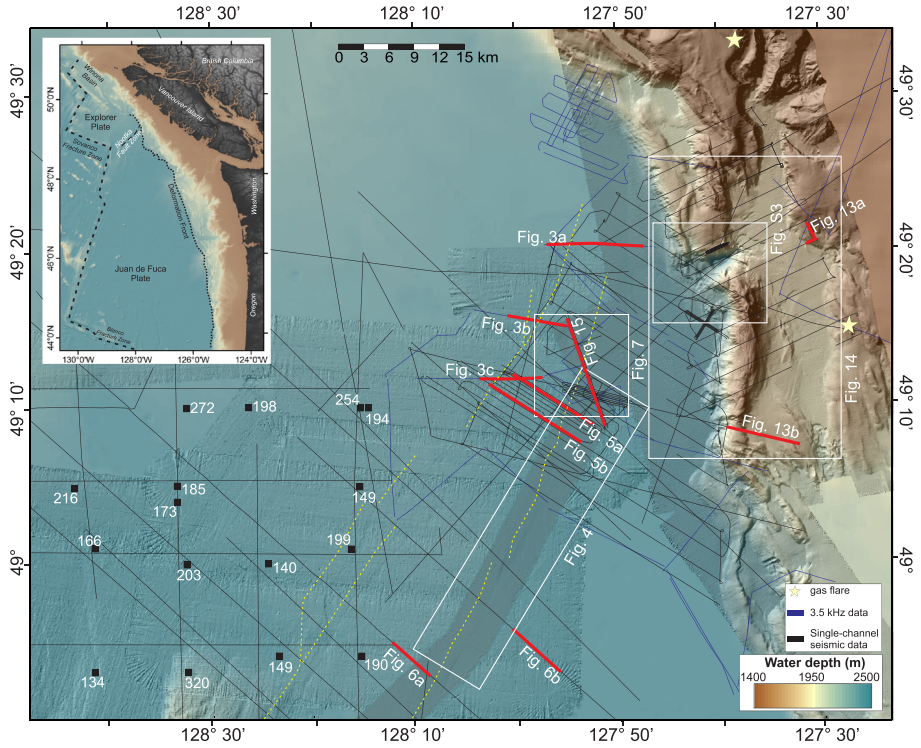


**Figure 1.** Bathymetry of the region along the Nootka fault zone with location of seismic and 3.5 kHz subbottom profiler data. Heat-probe stations with average heat flow values ($mW/m^2$) from Davis and Lister (1977a, 1977b) are shown by black dots. Surface traces of the two arms of the Nootka Fault zone are indicated by yellow dashed lines. Bathymetric depth shown is a collage from several multibeam surveys in the region (Delaney & Keck Team, 2003; Dziak, 2006; Mayer, 2001) and from data available through the Global Multiresolution Topography (GMRT) data set (Ryan et al., 2009). The image was created with ArcMap (V10.2) using the bathymetric data and background hill shading (illumination azimuth 315° and altitude 45°). Inset: Tectonic setting of the northern Cascadia margin. The Nootka fault zone is a left-lateral transform fault extending from the ridge near Middle Valley to the margin. It separates the Juan de Fuca Plate in the south and the Explorer Plate to the north. The deformation front (dotted line) is the first surficial deformation of the Cascadia accretionary sedimentary prism. The Juan de Fuca and Explorer Ridges and associated transform faults are shown as dashed lines.

Geophysical studies across the Nootka and Explorer region include seismic reflection imaging, heat flow studies (e.g., Davis & Lister, 1977a, 1977b; Hyndman et al., 1979; Rohr & Furlong, 1996), crustal refraction studies (e.g., Au & Clowes, 1982, 1984; McClymont & Clowes, 2005), seismic moment rate estimation of slip rate, and the thin effective seismic thicknesses (e.g., Hyndman & Weichert, 1983; Willoughby & Hyndman, 2005).

The complex evolution of the margin and plate boundaries of the Explorer plate, Nootka and Sovanco Fault zones, and the Winona Basin is the topic of ongoing scientific debate (e.g., Botros & Johnson, 1988; Braunmiller & Nábělek, 2002; Kreemer et al., 1998; Ristau, 2004; Rohr & Tyron, 2010; Rohr et al., 2018). About 4 Ma the Explorer ridge began to rotate clockwise (Botros & Johnson, 1988; Riddihough, 1984) and migrate to the west effectively separating the new Explorer plate from the Juan de Fuca. Shearing between the two plates has generated many steeply dipping faults, and, over time, much of this shearing has been localized in the NFZ (Rohr et al., 2018).

Two ocean bottom seismometer (OBS) and coastal station monitoring programs were conducted to map and characterize the seismicity of the region in 2010 (Riedel, Côté, Neelands, et al., 2014; Scherwath et al., 2011; Spence & Riedel, 2014) and 2014 (Riedel, Conway, et al., 2014; Riedel, Côté, Manning, et al., 2014). The results show very low seismicity levels across the Cascadia subduction zone off Vancouver Island with most events along the NFZ (Hutchinson et al., 2019; Obana et al., 2015). Earlier, the Nootka fault and slope region were the target of a project funded by the W.M. Keck foundation (e.g., Wilcock et al., 2007) in preparation for

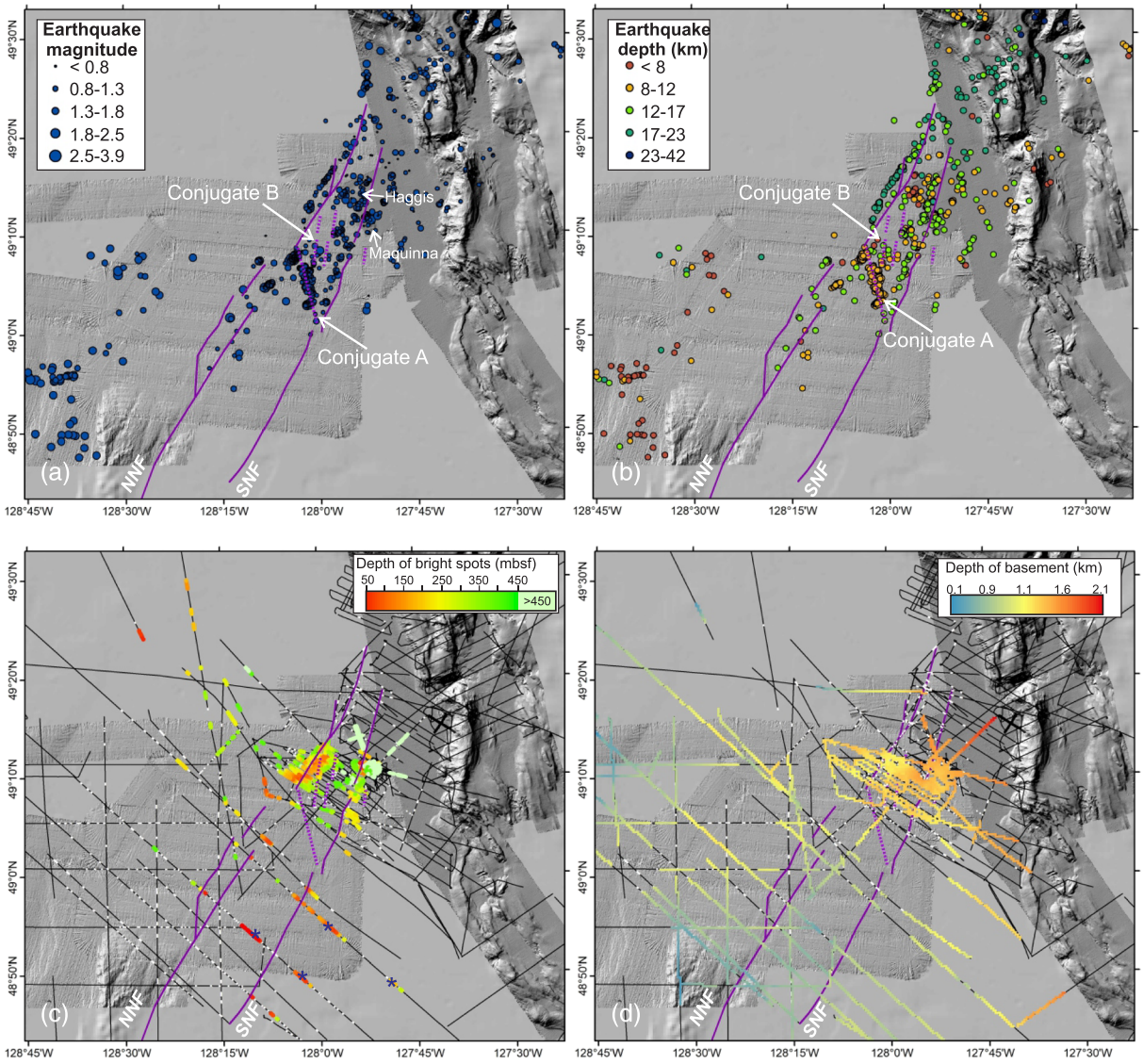


**Figure 2.** Map of the Nootka Fault zone traces (NNF = northern Nootka Fault; SNF = southern Nootka fault, (purple lines) as identified from bathymetry as well as single-channel seismic and 3.5 kHz data (line location shown as thin black lines). Shown are (a) locations of seismicity with magnitude proportional to symbol size (Hutchinson et al., 2019). (b) Earthquake hypocenter depth (Hutchinson et al., 2019), (c) depth of bright spots below seafloor (those highlighted by an asterisk are described as BSR-like events in section 3.4), and (d) basement depth below seafloor. Locations of small sediment-hosted faults identified in seismic and acoustic data are shown as short white line segments in (c) and (d). Conjugate Fault Set A is based on earthquake studies (Hutchinson et al., 2019), and Conjugate Fault Set B is based on this study. A detailed view of the region southwest around the two seafloor mounds is given in Figure S5.

the NEPTUNE regional offshore cable observatory (North East Pacific Time series Underwater Networked Experiment), now part of University of Victoria Ocean Networks Canada (ONC). ONC now has an extensive array of seafloor monitoring instruments in the region (https://www.oceannetworks.ca/). During the installation and recovery of seafloor instrumentation, new observations of seafloor morphology (cold vents and carbonate formations) were made, followed by investigations by the Geological Survey of Canada and the University of Victoria (e.g., Spence & Willoughby, 2004; Willoughby & Fyke, 2003).

This work included multibeam seafloor swath surveys in 2001 with the R/V Thomas G. Thompson (Delaney & Keck Team, 2003; Mayer, 2001) that led to the discovery of two seafloor mound structures (named Haggis and Maquinna) along the NFZ (Riedel et al., 2001). Higher-resolution EM300 multibeam swath bathymetry data were subsequently acquired in 2002 with a transect along the southern arm of the NFZ.

Here we compile results and link observations from previous expeditions to the region to describe the nature of fluid flow along the NFZ. We include single channel seismic reflection and 3.5 kHz subbottom profiler imaging conducted over six cruises since 1994 (see Figure 1 for line locations), two multibeam seafloor bathymetry mapping surveys, remotely operated vehicle (ROV) dives undertaken during deployment and recovery of seabed instrumentation, water-column profiling, and piston coring at Maquinna mound. We integrate these observations with a previous regional heat flow probe survey (Davis & Lister, 1977a, 1977b). By combining data and analyses from >20 years of research, this study provides a detailed depiction of the NFZ, and associated fluid flow processes, seafloor mound formation, and occurrences of gas hydrates on the Nootka slope region.

This investigation addresses the general nature of fluid flow in the region of the NFZ: (1) What is the possible origin for the fluids and are there linkages to deeper processes such as mantle serpentinization? Specifically, we address these questions: (2) Why are seismic bright spots regionally restricted to a narrow zone along the fault trace? (3) What is the origin of the two seafloor mounds uniquely located on the abyssal plain along the Cascadia margin close to the fault traces? (4) What created the unique seismic character and bathymetric shape of the seafloor mounds? (5) What is the source of fluids expelled at Maquinna mound? (6) Are gas hydrates occurring along the Nootka slope region indicated by bottom-simulating reflectors (BSRs) and can their depth and seismic expression be used to infer regional heat flow?

Results from our study have implications for hazard assessments of the region. These include assessment of the occurrence and rupture area for mega-thrust earthquakes along the Explorer plate (e.g., Gao et al., 2017, 2018) by providing heat flow estimates on the Nootka slope, evaluating the potential for slope failures through mapping gas hydrate and cold vents across the Nootka slope (e.g., initiated by Riedel et al., 2018), and estimating the stress orientation along the Nootka fault trace from en échelon mini basins seen in multibeam seafloor images compared to other regional stress analyses (e.g., Govers & Meijer, 2001; Ristau et al., 2006).

## 2. Materials and Methods

Single-channel seismic survey data were collected during six expeditions (line coverage in Figure 1) with varying data acquisition parameters according to unpublished cruise reports: Three cruises from 1994 to 1996 were conducted by the Geological Survey of Canada (Rohr & Furlong, 1996), and three cruises were conducted in 2001, 2003, and 2004 as collaboration between the Geological Survey of Canada and the University of Victoria (Spence & Willoughby, 2004; Spence et al., 2001; Willoughby & Fyke, 2003). The seismic data were acquired using single airguns of varying sizes and a short single-channel streamer. Data processing of the seismic data used for this study included a band-pass filter to reduce noise, deconvolution to remove the air gun bubble pulse, correction for spherical divergence, and time migration. Data from the 1994–1996 cruises were affected by 50 Hz noise, and therefore, a low-cut 50 Hz filter was applied prior to the other processing. In 2001–2004, the streamer consisted of a 25 m active section and was towed approximately 40 m behind the vessel giving nearly zero-offset data. Therefore, only regional velocity information from previous wide-spacing multichannel and refraction surveys is available for migration (Au & Clowes, 1982; Hasselgren & Clowes, 1995; McClymont & Clowes, 2005). Velocity was defined to start at 1,500 m/s at the seafloor and a gradual increase to 1,800 m/s at 1 km was used to approximate the gradual increase in velocity with depth (Au & Clowes, 1982). It should be noted that the sediment velocity can be impacted by the presence of fluids and/or free gas, which we cannot include in our time migration of the data due to the lack of velocity control from multichannel seismic or OBS data across the regions affected.

All seismic data are then used to identify sediment-hosted faults from the time-migrated seismic sections. Faults are identified by vertical offsets of sedimentary reflectors. In these high-frequency single-channel reflection profiles, offsets of a few ms can be detected. Horizontal resolution, however, may be on the order of 100 m (Rohr et al., 2018). Bright spots are identified from the data as high-amplitude anomalies (minimum twice the reflection amplitude when compared to reflection strength of adjacent seismic traces) and mapped regionally. The BSR as indicator for the presence of gas hydrates was identified from the seismic data as a polarity-reversed event (compared to seafloor reflections) that crosscuts the regular stratigraphy. The 3.5 kHz subbottom profiler data were not further processed or migrated. The instantaneous amplitude (envelope) is used for display purposes and analysis (e.g., fault picking).

Seafloor multibeam swath bathymetry data were collected during two expeditions. The first survey in 2001 with the R/V Thomas G. Thompson (Mayer, 2001) yielded low-resolution but full-coverage images of both arms of the NFZ. During this cruise, water-column data at the Maquinna mound were acquired with a conductivity temperature depth (CTD) profiler equipped with oxygen, optical backscatter, and light-transmission sensors. Higher-resolution multibeam data were subsequently acquired over the southern arm of the NFZ in a single swath from the Nootka slope and seafloor mound Maquinna to Middle Valley at the northern end of the Juan de Fuca mid-ocean ridge system. A piston core sample was taken from the Maquinna mound during expedition PGC01-003 as well as water-column data using a CTD profiler to verify the earlier measurements from the R/V Thomas G. Thompson (Spence et al., 2001). The ROV Tiburon made one dive transect (Dive 472) in August 2002 across the Maquinna mound yielding video footage of chemosynthetic communities associated with areas of fluid expulsion. Additional bottom video footage with the ROVs ROPOS and Tiburon was obtained from several dives at the toe of the Nootka slope as part of the Keck Project (e.g., Wilcock et al., 2007). Only still images were used for this study together with the short dive descriptions and navigation. The dive tracks and image locations were compared with the bathymetry from the multibeam surveys by using the recorded depth of the ROV to check for navigation errors. To within the horizontal and vertical resolution limits of ~50 and ~10 m, respectively, of the multibeam data, the depth-track of the ROV and multibeam-based depth-chart are identical.

With the limited regional sediment velocity-depth information, we used the BSR, which is taken to be at the base of gas hydrate stability (structure one, sI) to estimate heat flow values for the slope region. There are no existing heat-probe data for comparison. We followed the computation steps outlined in previous BSR heat flow studies on the Cascadia margin (Ganguly et al., 2000; He et al., 2007; Riedel, Tréhu, et al., 2010). The difference in travel times of the seafloor and BSR ($\Delta T_{BSR}$) are converted to BSR-depth ($D_{BSR}$) using a simple velocity function ($V = 1511 + 521 \cdot \Delta T_{BSR} - 93\ \Delta T_{BSR}{}^2$). The velocity function does not consider velocity increases due to high-velocity gas hydrate. The estimated heat flow is not sensitive to the velocity-depth function, since a change in BSR depth results in a change in BSR temperature without significantly changing the temperature gradient. Hydrostatic pressure at the BSR was calculated using a constant water density (1,030 kg/m$^3$). Temperatures at the BSR were estimated from the phase boundary in the gas hydrate stability field using sI methane hydrate and a constant pore water salinity of 34 ppt. The phase-boundary equation was adapted from Englezos and Bishnoi (1988). Seafloor temperatures as function of water depth were determined as outlined by He et al. (2007). The empirical expression for thermal conductivity ($\kappa$) versus depth given by Davis et al. (1990) is used ($\kappa = 1.07 + 5.86{\cdot}10^{-4} \cdot D_{BSR} - 3.24{\cdot}10^{-7} \cdot D_{BSR}{}^2$). Heat flow values were calculated assuming a linear conductive temperature gradient. Combined uncertainties from the various input parameters are estimated to be 20%, following procedures and calculations given by Ganguly et al. (2000), He et al. (2007), and Riedel, Tréhu, et al. (2010).

The piston core pore waters were analyzed for sulfate, chloride, methane, and ethane concentrations, as well as methane stable carbon isotope ratios, following Lapham et al. (2008). Briefly, subsamples were collected every 10 cm for the first 50 cm, every 20 cm for 1 m, and every 50 cm to the bottom of the core. For sulfate and chloride analyses ~8 ml of sediment was placed into centrifuge tubes to separate pore water from sediment. The supernatant was then diluted 1:100 with deionized water and injected into a Dionex™ ion chromatography (IC) system (Sunnyvale, California) to determine sulfate and chloride concentrations compared to a certified IAPSO seawater standard. For methane and ethane concentrations, a 3 ml sediment plug from each section was immediately placed into a 20 ml glass serum vial. These plugs were also used to determine porosity by weighing the sample before and after drying (assuming identical grain density and constant volume). Using a headspace equilibration method, the headspace was subsampled and injected into a Shimadzu Mini II Gas Chromatograph (Kyoto, Japan) equipped with a flame ionization detector and Porapak Q™ analytical column. Sample areas were then compared to certified gas standards and converted to dissolved methane concentrations using solubility equations (Magen et al., 2014). Concentrations should be considered minimums as the cores will have degassed upon ascent through the water column. Methane ($C_1$) to ethane ($C_2$) ratios ($C_1/C_2$) were calculated from raw ppmv values. For all concentration measurements, the precision for replicate measurements of single samples was ±3%. For methane stable carbon isotopes, a second aliquot of the headspace was collected and injected into a Finnigan-MAT 252™ gas chromatograph/isotope ratio mass spectrometer and reported $\delta^{13}C\ (\%) = (R_{sample}/R_{standard} - 1) \times 1{,}000$, where $R_{sample}$ and $R_{standard}$ are the $^{13}C/^{12}C$ ratios of the sample and PDB standard, respectively.

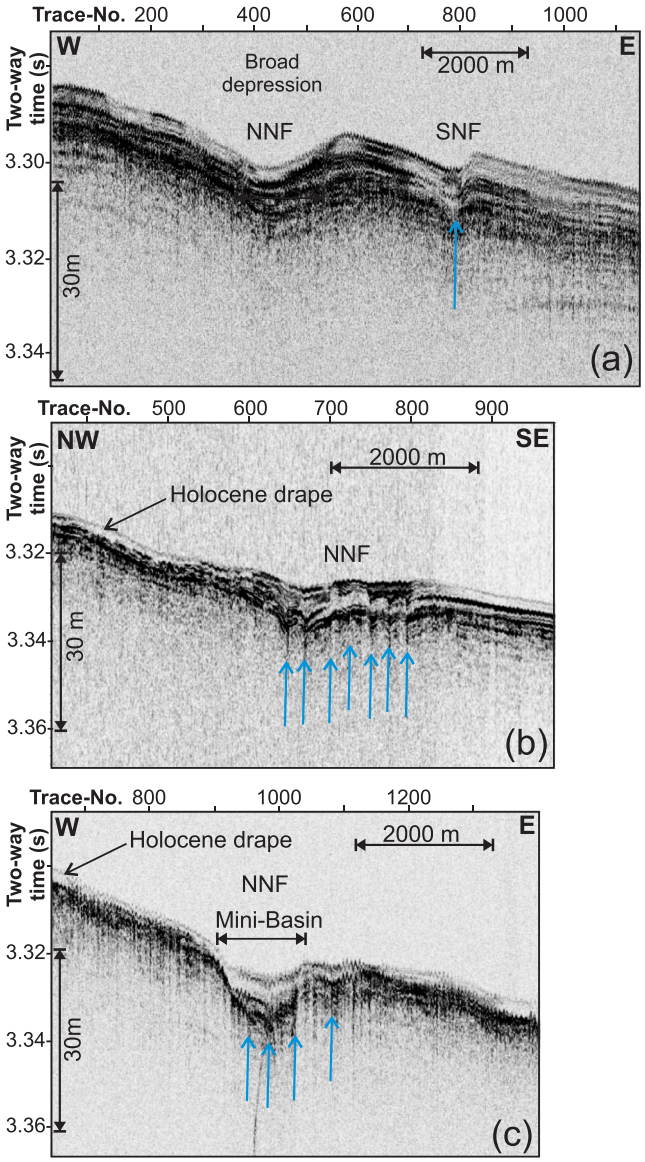


**Figure 3.** Examples of 3.5 kHz data across the Nootka Fault zone showing the occurrence of minibasins with dense small-scale faulting (blue arrows) and the evolution into more broad depressions with no visible fault due to high sedimentation rates near the deformation front. Holocene drape is seen along all lines, thicker in the minibasins. Line locations are shown in Figure 1. Vertical exaggeration is 80.

Mixing lines for a Bernard genetic diagram (Bernard et al., 1978) were calculated using the $\delta^{13}C$ values and C1/C2 ratios of microbial, thermogenic, and abiotic endmembers. The $\delta^{13}C$ of the mixtures ($\delta_{mix}$) were calculated as

$$\delta_{mix} = f_A * \delta_A + f_B * \delta_B,$$

where $f_A$ and $f_B$ are the fractional contributions from each endmember and $\delta_A$ and $\delta_B$ are the $\delta\ ^{13}C$ values of the endmembers. The microbial endmember is calculated as the average $\delta\ ^{13}C$ (−83.1‰) of the most $^{13}C$-depleted methane from IODP Expedition 311 Sites U1325 and U1326 (Pohlman, Kaneko, et al., 2009). The thermogenic endmember is calculated as the average $\delta\ ^{13}C$ (−44.0‰) from Barkley Canyon seep methane (Pohlman, Bauer, et al., 2009; Pohlman et al., 2005). The abiotic endmember is calculated as the average $\delta\ ^{13}C$ (−8.3‰) of abiotic methane from peridotite-hosted fluid inclusions (Grozeva et al., 2020). The $C_1/C_2$ values for the mixtures were calculated with a similar mixing model approach that used the $C_1/C_2$ ratios of the microbial (85,650), thermogenic (41), and abiotic (387) endmembers instead of the endmember $\delta\ ^{13}C\text{-}CH_4$.

## 3. Results

### 3.1. Traces of the NFZ

Two distinct zones of faulting along the NFZ were previously interpreted in the study by Hyndman et al. (1979) from single-channel and 3.5 kHz subbottom profiler data. The fault traces were subsequently remapped in more detail using multibeam data from 2001 and 2002 (Rohr et al., 2018). In this study we additionally interpret detailed seismic surveys around both fault traces and the seafloor mounds. The main trend of the NFZ is from the SW to the NE (with an azimuth of 30–40° measured clockwise). The two fault traces converge landward (Figure 2) and shift to the North as they approach the slope. There is pervasive faulting of the sediments over the NFZ, but the density of faulting diminishes landward (Rohr et al., 2018). Also, faulting along the two major traces (seen by V-shaped depressions on seismic sections) is limited to deeper sediment sections close to the deformation front, which is linked to a thicker sediment cover and deeper basement (e.g., Figure 6 in Rohr et al., 2018).

Detailed earthquake locations computed from a 3-month OBS deployment also delineate the fault traces (Hutchinson et al., 2019), but the projected hypocenter locations appear shifted by a small amount, ~2.5 km, to the NW relative to the seafloor traces (Figures 2a and 2b). There is a regional difference in earthquake occurrence: Most events were located north of the Conjugate A fault set (Hutchinson et al., 2019), and not as much seismicity was recorded south of there (Figure 2a). The northern arm of the NFZ shows earthquake depths of around 16–23 km, deeper than those along the southern arm (~12–16 km; Figure 2b). The conjugate faults (azimuth ~165°) were defined by Hutchinson et al. (2019) and Rohr et al. (2018), and a prominent cluster of earthquakes delineating this trend shows shallower depths of ~8–12 km. Tracing individual faults from line to line, we were able to define a possible second set of conjugate faults (labeled "Conjugate B" in Figures 2a and 2b) trending with an azimuth of ~10° (dashed purple lines in Figure 2).

The 3.5 kHz data reveal that the main fault traces at the surface are made up of numerous small-scale faults (Figure 3). On the subbottom profiler line shown in Figure 3b, seven small faults are seen disrupting the sediments up to the seafloor. The distance between the minifaults is a near constant 250 m. The seafloor

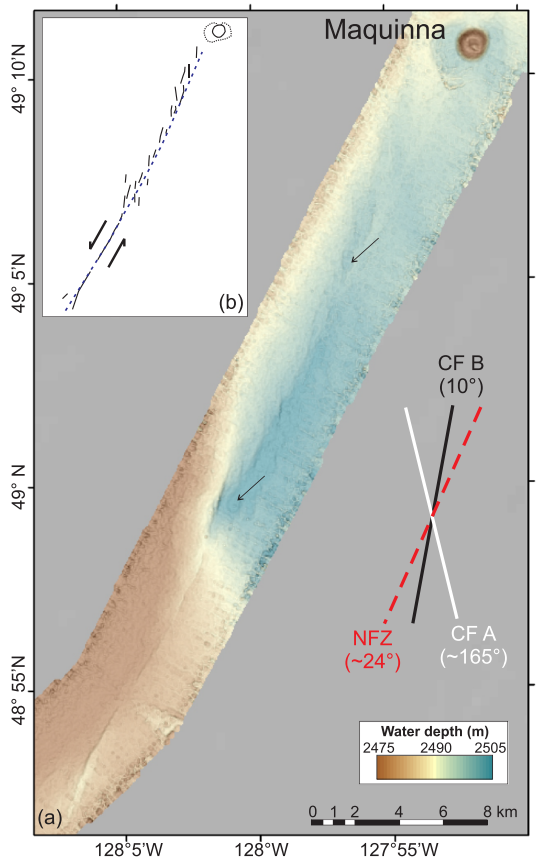


**Figure 4.** (a) Multibeam data and (b) line drawing of the lineation seen along the southern arm of the Nootka Fault trace, SW of the Maquinna mound. The strike of the main fault is ~24° clockwise from north (red dashed line) based on the bathymetry data. Smaller faults are rotated by 10°–15° from the main fault trend. They correlate well to the Conjugate Fault (CF) A from earthquakes data (white line) as defined by Hutchinson et al. (2019) and Ristau et al. (2006) and CF B from seismic data (black line) shown in this study (compare to Figures 2a and 2b). Teardrop minibasins develop along the fault trace, shown by small black arrows.

expression of the two main NFZ traces can only be identified eastward as far as the two seafloor mounds Haggis and Maquinna. The subbottom profiler data east of the mud volcanoes show only a broad depression for the northern fault trace (NNF; Figure 3a).

### 3.2. Pull-Apart Minibasins Along Nootka Fault Trace

High-resolution multibeam data along the southern arm of the NFZ show that the main fault is disrupted into S-shaped en échelon segments, which create small depressions or minibasins. This behavior is expected for left step overs on left-lateral faults (Dooley & Schreurs, 2012). The high-resolution multibeam data acquired along the southern trace of the NFZ provide a detailed view of the development of small pull-apart basins (Figure 4). Along the main fault trend (striking ~24° clockwise from North), a series of teardrop-shaped minibasins, up to 8 m deeper than the surrounding seafloor, have developed. Smaller offset faults can also be identified, rotated 10–15° away from the main fault trend. Similar basins are likely occurring along the northern Nootka fault arm as well, but bathymetry is too coarse to see such details. Minibasins are identified on the northern trace only from 3.5 kHz subbottom profiler data (Figure 3). Thus, the NNF likely also consists of left stepping segments. En échelon left stepping fault segments associated with extensional minibasins confirm the previously interpreted left-lateral strike-slip motion. Their orientation yields a maximum horizontal stress axis oriented at ~190° (clockwise from North), which compares well to orientations of 170–180° derived from earthquake moment tensors (Braunmiller & Nábělek, 2002; Ristau et al., 2006).

### 3.3. Bright Spots, Faulting, and Basement Topography

Bright spots are seen on either side of the two main NFZ traces in the seismic data (Figures 2c and 5) along 3–4 km of each of the fault arms. It is noteworthy that the Conjugate A fault system by Hutchinson et al. (2019) is not associated with bright spot development. The bright spots occur at 120–400 ms two-way time (TWT) below seafloor, approximately 100–340 m below seafloor (bsf) using a velocity of 1,700 m/s appropriate for these shallow reflections. They are conformable to the sedimentary layers and vary in extent across the fault from a few 100 m to 4 km. Individual layers appear to become suddenly bright in reflection amplitude. Where occurring as an isolated reflection (and not as stack of closely spaced reflections), these bright spots have a polarity opposite to the seafloor, representing a decrease in impedance; the conformable sediment layers have regular polarity and amplitude outside of the bright spots. Over the lateral extent across the fault and along the bright spots, there also is a reduction in their frequency content. Apparent sediment deformation at the two Nootka fault traces is typically in the form of V-shaped depressions (Figure 5).

As noted by Hyndman et al. (1979) and Rohr et al. (2018), around and between the two Nootka fault traces, there is a basement high of up to 400 m. We added basement depths from the tightly spaced seismic sections around the seafloor mounds (Figure 2d). The basement depth below seafloor gradually increases landward as expected from a higher sediment input due to the proximity to the slope and onset of subduction. As well, basement topography along the northern and southern arm of the NFZ is higher, coincident with the bright spot locations shallowest beneath seafloor.

Our reflection seismic data suggest an apparent eastern limit in bright spot occurrence (Figure 2c); however, lines on the abyssal plain east of the mounds are truncated at 3.9 s TWT, as no deep water delay was used in the recordings. With average water depths of 3.4 s TWT, our observations are limited to ~ 0.5 s TWT or ~400 m bsf. Within this limit, we infer that bright spots are no longer occurring at these shallow subseafloor depths.

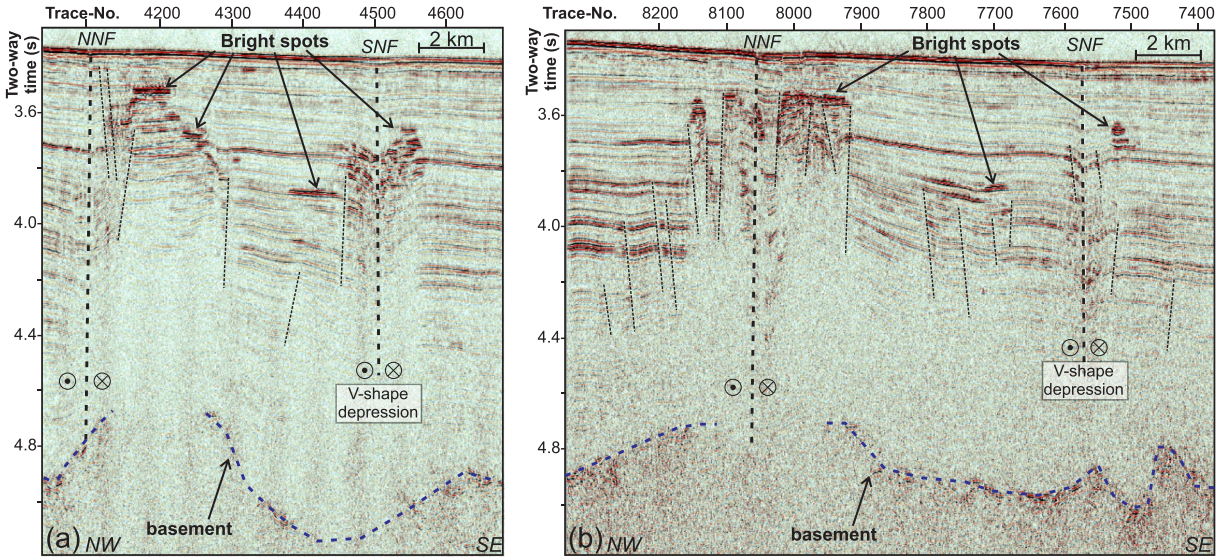


**Figure 5.** Example of single-channel seismic lines crossing the north (NNF) and south (SNF) Nootka fault trace with typical development of V-shape depressions and bright spots conformable to the surrounding sediments. The tops of the bright spots show reversed polarity relative to the seafloor indicating a downward reduction in acoustic impedance. Below the bright spots, the reflections are often reduced in amplitude and frequency. Basement (blue dotted line) shows some substantial elevation changes close to and beneath the NNF. Vertical exaggeration is ~10.

### 3.4. Cross-Cutting, BSRs on the Abyssal Plain

Single-channel seismic data acquired on the abyssal plain ~25–30 km west of the toe of the Nootka slope show several unusual high-amplitude reflections within and adjacent to the NFZ and up to 28 km SE from the SNF (Figure 6). These high-amplitude reflections occur within the shallow laminated sediment sequences, ~50–120 ms TWT below seafloor (<100 m bsf) over 4–5 km-long patches, but line spacing does not allow detailed mapping. The polarity of these reflections appears opposite to that of the seafloor; they crosscut the otherwise seafloor parallel layering and have smooth morphology. They further show high-amplitude brightening underneath and some possible low-velocity sag. Overall, they appear similar to BSRs seen in gas hydrate environments; yet they are not strictly bottom simulating. This is in contrast

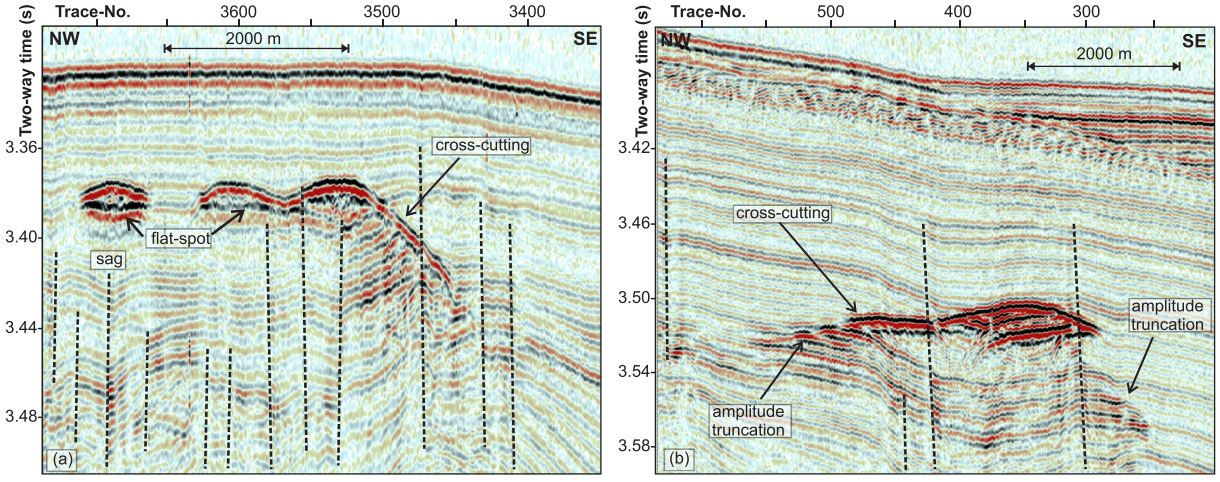


**Figure 6.** Examples of unusual reflections across minor fault traces (dashed black lines) across the abyssal plain (location see Figure 1). These reflections are characterized by a polarity opposite to the seafloor, brightening of underlying sediment layers, and crosscutting of the mostly seafloor-parallel sediment layers. They are somewhat similar to deep water marine BSRs, which are associated with gas hydrates. Note also the development of flat spots and low-velocity sags underneath the BSR-like features, indicative of a gas-water contact. Left section is between the northern (NNF) and southern (SNF) Nootka fault trace; right section begins 2.5 km southeast of the SNF. Vertical exaggeration is 30.

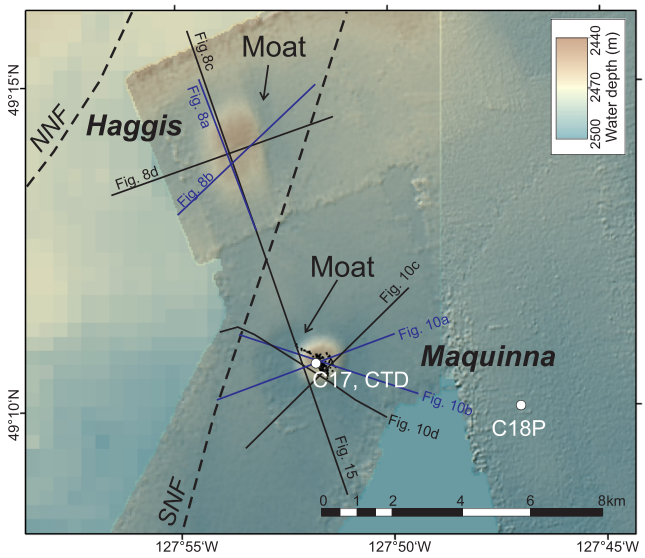


**Figure 7.** Bathymetry of the two seafloor mounds Haggis and Maquinna. Shown also are the CTD station (Figure 11), piston cores C17 and C18P (Figure S1), and ROV positions from the Tiburon Dive 472 (black dots). The traces of the southern and northern arm of the Nootka fault zone (SNF and NNF) are indicated by dashed lines.

to bright spots described above near the Nootka fault traces, which are conformable to sedimentary layering (Figure 6), disrupted, produce diffractions, and mask reflectors below. In total, four distinct locations across the study region were noted where these unusual reflections occur (see Figure 1).

### 3.5. Seafloor Mounds

A multibeam imaging survey in 2001 across the Nootka slope and fault zone region (Mayer, 2001) revealed two seafloor mounds that were subsequently investigated using seismic reflection imaging and piston coring (Riedel et al., 2001). The two features, called Maquinna (southern mound) and Haggis (northern mound), appear to be slightly offset to the south from the seafloor expressions of the two fault traces (Figure 7).

#### 3.5.1. Haggis Seafloor Mound

The Haggis mound is an elongated feature 3.5 km N-S by 2.0 km E-W, excluding the moat (Figure 7); it appears to consist of two conjoined circular features. The maximum height is ~30 m above the surrounding seafloor. A semicircular moat has formed around the mound, and, although only partially mapped with the multibeam data, it appears deeper and wider on the southern and western flank in seismic and 3.5 kHz subbottom profiler data (Figures 8 and 9). The western moat is ~15 m deep and shows an acoustically transparent fill on top of the regional stratigraphy. The top of Haggis mound appears to be cut by a series of faults as seen on the 3.5 kHz data (Figures 8a and 8b), which is corroborated by the seismic reflection data (Figures 8c and 8d). Along the fault trace, there are several smaller amplitude reflection anomalies that suggest upward migration and local trapping of fluids. The 3.5 kHz and single-channel seismic reflection data reveal regular sediment layering beneath the mound with progressively steeper downward dip associated with the southern arm of the NFZ, which is seismically seen as a V-shape depression that becomes more pronounced with depth. The seismic data show that the mound is underlain by a high-amplitude zone of overlapping reflectors (Figures 8c and 8d), at 640–800 m bsf (Figure 9a) that are conformable to the sediment layering above. The first reflector shows a polarity opposite to that of the seafloor, so impedance decreases downward. Some faint reflections suggest that layers below the bright spot are conformable to those above. Several small-scale amplitude anomalies were also imaged beneath the main high-amplitude reflective zone possibly indicating a feeder-channel for upward migrating fluids (between 4.25 and 4.45 s TWT and traces 150–250; Figure 8c).

#### 3.5.2. Maquinna Mound

The Maquinna mound is located ~6 km south-southeast of Haggis, and 2 km south of the south fault trace (Figure 7). The circular mound is ~2.5 km in diameter, is ~40 m above the surrounding seafloor, and has a central caldera that is depressed by ~8 m (Figure 7). An almost symmetrical circular moat ~15 m deep is filled with acoustically transparent sediments (Figures 10a and 10b). As seen in the 3.5 kHz data, the sediments next to the fault are uplifted by 2–3 m before plunging into the moat surrounding Maquinna (Figures 10a and 10b). Although nearly acoustically transparent, the moat shows some small-scale reflections, possibly indicating mud flows. The seismic reflection data show that beneath Maquinna, the faintly imaged sediment layers are seafloor-parallel (Figures 10c and 10d). The poor image is likely due to the steep dip of the central mound and the geometry of a short streamer in deep water. The apparent acoustic masking could be an imaging artifact of the convex shape. As seen at Haggis, Maquinna is also underlain by a bright amplitude reflective zone (Figures 10c and 10d) about 400 m bsf (Figure 9b). It is truncated in the NW at the boundary of the SNF trace. The reflective zone is made up of several smaller reflector segments possibly opposite in polarity relative to the seafloor that are not conformable to the sediment layering. Polarity is more difficult to identify for the deep reflective zone compared to Haggis, as reflectors are more rugged in nature. This is different from Haggis mound where the deep high-amplitude zone is mostly conformable to the sediment layering. Faulting at Maquinna reveals a ring-like pattern outlining the shape of the donut-like seafloor expression. Two rings of faults are seen as well as a set of NE-SW trending faults cutting through the bright amplitude reflection (Figure 9b). Locations of faults that intersect a TWT of 4.1 s were plotted and reveal ring-shaped patterns (Figure 9b).

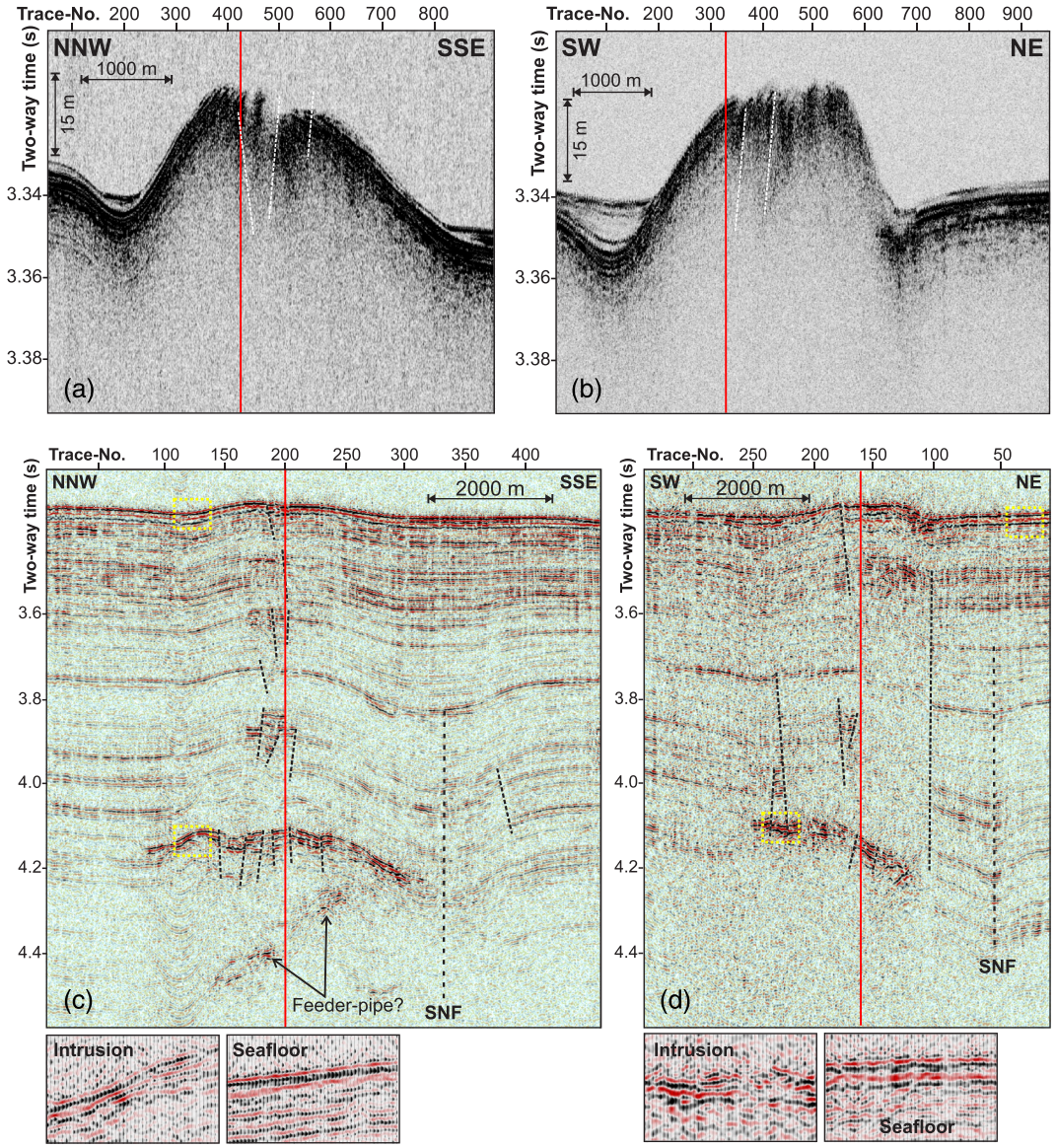


**Figure 8.** Subbottom profiler data across Haggis mound in (a) NNW-SSE and (b) SW-NE orientation. Note the rough top that may be faulted (white dashed lines), as well as a sediment layer traced continuously from outside the mound, underneath the moat, and onto the top of the mound structure. Vertical exaggeration is 45. Single channel seismic reflection data across Haggis mound: (c) NNW-SSE and (d) SW-NE orientation. The bright spot 0.8 s two-way time (~680 m) below the seafloor is mostly conformable to sediment layering. Vertical exaggeration is 12. Yellow dotted boxes are shown in lower panel to illustrate polarity of the reflection from the seafloor and the intrusion. Locations of all lines are shown in Figure 7. Red line marks crossing point of the lines.

During repeat expeditions, including the two SeaJade OBS experiments, the 12 kHz echo sounders were used to identify gas plumes in the water column. No acoustic anomalies were observed in the water column in 2010, 2013, and 2014. However, in 2001 water-column chemical and physical data were acquired indicating discharge of warm fluids from the Maquinna mound (Figure 11). The CTD data reveal a reduction in light transmission coincident with an increase in backscatter, increase in temperature (+0.005°C), and reduction in oxygen (−0.15 mg/L).

A piston core (C17) from the center of Maquinna defined pore water sulfate, chloride, porosity, and dissolved gas trends within the mound (Figure S1 in the supporting information). Chloride values fluctuate around a mean seawater value of 550 mM, whereas sulfate values decrease downcore, with a relatively low value

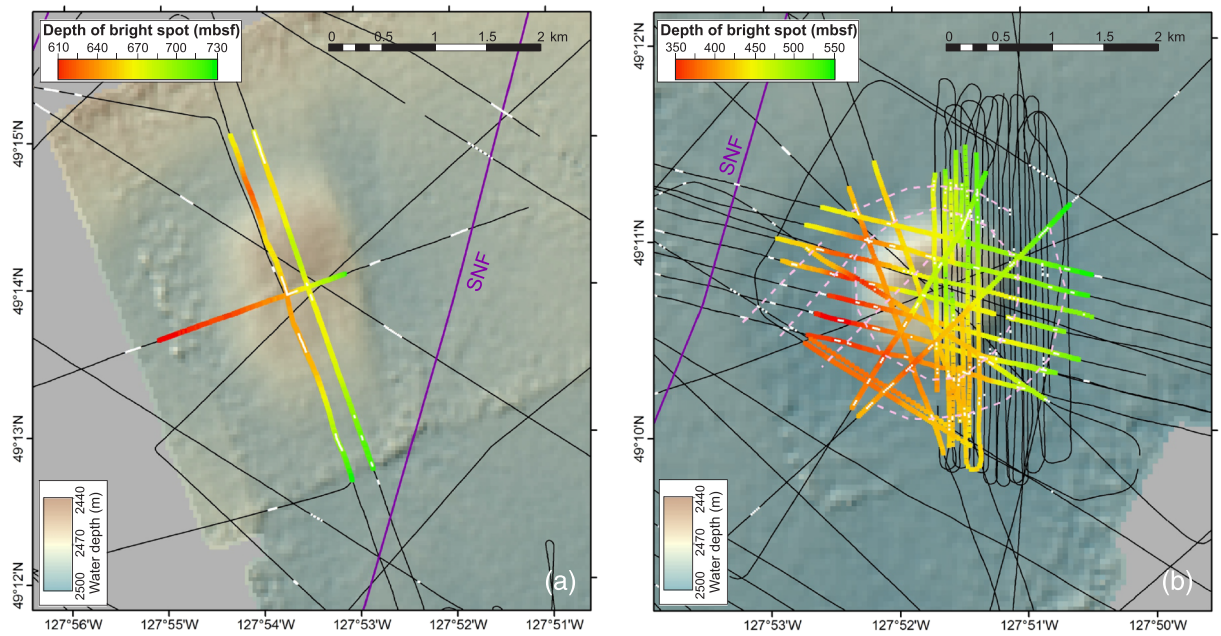


**Figure 9.** (a) Depth of bright spot underneath Haggis. Although data coverage is sparse, the data suggest dipping of the bright spot from west to east. (b) Depth of bright spot underneath Maquinna. The bright spot dips from west to east (by ~200 m). The mound feature is surrounded by two rings of faults (pink dashed lines) as well as a set of SW-NE trending faults. Location of ring faults are shown at a depth of 4.1 s (two-way time). SNF = southern arm of the Nootka fault zone. Black lines are ship track as in Figure 7; white line segments depict fault locations as in Figure 2c.

(13 mM) at ~40 cm bsf and sharp decrease between the depths of 250 and 310 cm bsf. Porosity decreases downcore from a near-seafloor layer of at least 2 m thickness with values of ~0.7 to around 0.5 for the remainder of the core. Methane concentrations increase with increasing depth at 250 cm bsf, the depth above which sulfate concentrations began to decrease. Decreasing sulfate where methane concentrations increase is consistent with the microbially mediated anaerobic oxidation of methane (AOM) occurring at the sulfate-methane transition zone (SMTZ) (Boetius et al., 2000; Hoehler et al., 1994). Methane with $\delta^{13}C$ values uniformly less than −72‰ indicates a microbial origin for methane (Figure 12; Whiticar, 1999). Ethane was detected at relatively high concentrations, and the ratio of methane to ethane ($C_1/C_2$) shows values all lower than 500 (Figures S1f and 12). The minimum $\delta^{13}C$ value −90.5‰ for methane within the SMTZ is consistent with carbon isotope exchange during sulfate-limited AOM (Yoshinaga et al., 2014), which is achieved under steady-state conditions (Chuang et al., 2019). To maintain near-seawater sulfate concentrations under steady-state conditions to 2.5 m bsf requires continuous downward advection of seawater, which may be driven by a tidal-pumping process previously observed by Labonte (2007) at the Maquinna mound.

Pore water profiles of chloride, methane, and sulfate at the abyssal plain core site (C18P), located 40 km from Maquinna mound, are similar to those reported for off-seep profiles at the Bullseye vent site (IODP Site U1328) on the central northern Cascadia accretionary prism (~95 km to the southeast), where sulfate concentrations gradually decrease with depth to greater than 6 m below the seafloor (Pohlman et al., 2013). Methane concentrations remain low throughout the core, and similar to C17, chloride concentrations fluctuate around seawater values. Porosity is equally layered at the reference site as for the core at Maquinna suggesting that no major sedimentologic effect is impacting the geochemistry of the cores.

### 3.5.3. ROV Bottom Video Survey

Across the Maquinna mound, a video transect was carried out with the ROV Tiburon in 2002 (Dive TN 472). Seafloor video imagery revealed several white galatheid crabs (squat lobsters; Figure S2) as commonly seen at hydrothermal vents (e.g., Schreier & Lutz, 2019), but overall, the diversity of seafloor fauna was limited. At several locations, clam-shell debris (*Solemya riedi*), typical for hydrogen-sulfide ($H_2S$) rich environments, was seen but otherwise no indication of vent-flora and fauna or carbonate crusts indicative of active gas discharge.

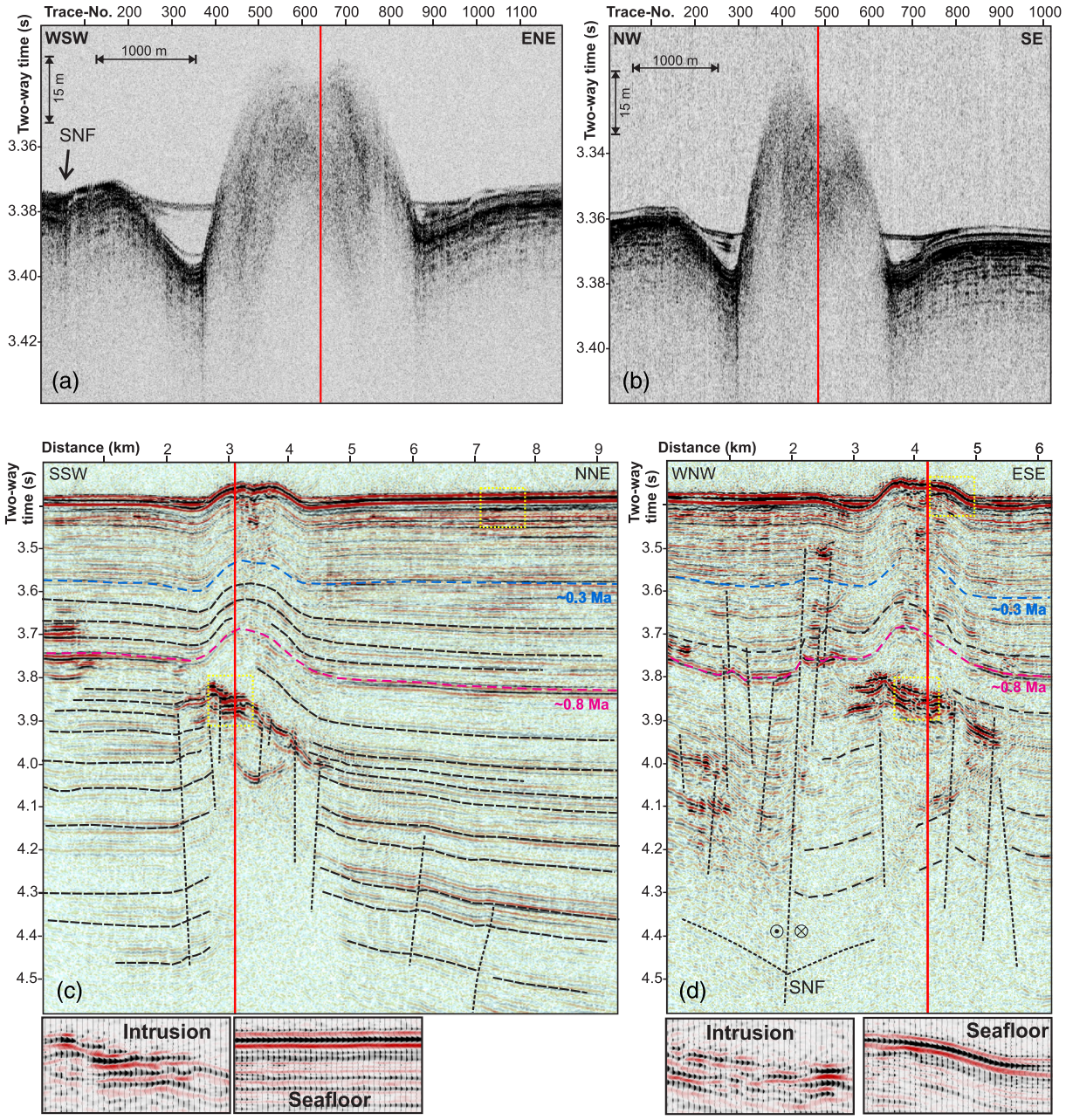


**Figure 10.** Subbottom profiler data across Maquinna mound in (a) WSW-ENE and (b) NW-SE orientation. Note the deep moat and steep top that is poorly imaged with the 3.5 kHz system. Sediment layers can be traced from outside the mound beneath the moat that are interpreted to continue up to the top of the mound. Vertical exaggeration is 45. Single channel seismic data across Maquinna mound: (c) in SSW-NNE and (d) WNW-ESE orientation also crossing the southern Nootka fault trace (SNF) at ~2 km along the line. Vertical exaggeration is 12. Two horizons with approximate ages (from Rohr et al., 2018) are superimposed together with fault interpretation. The high-amplitude feature underneath the mound is irregularly shaped and asymmetric to the donut-shape seafloor expression (see Figure 9b). Yellow dotted boxes are shown in lower panel to illustrate polarity of the reflection from the seafloor and the intrusion. For all locations, see Figure 7. Red line marks crossing point of the lines.

### 3.6. Gas Hydrates, Cold Vents, and Bottom Simulating Reflectors on the Nootka Slope

Seismic reflection data in the Nootka region included a systematic survey of the Nootka continental slope in 2003 (Willoughby & Fyke, 2003) as well as two additional lines crossing the slope from the shelf to the abyssal plain collected in 1995 (Figure 1). The seismic data are not able to image the sediment structure under the steep topography of the individual ridges; however, on more gentle slopes, there is sufficient resolution

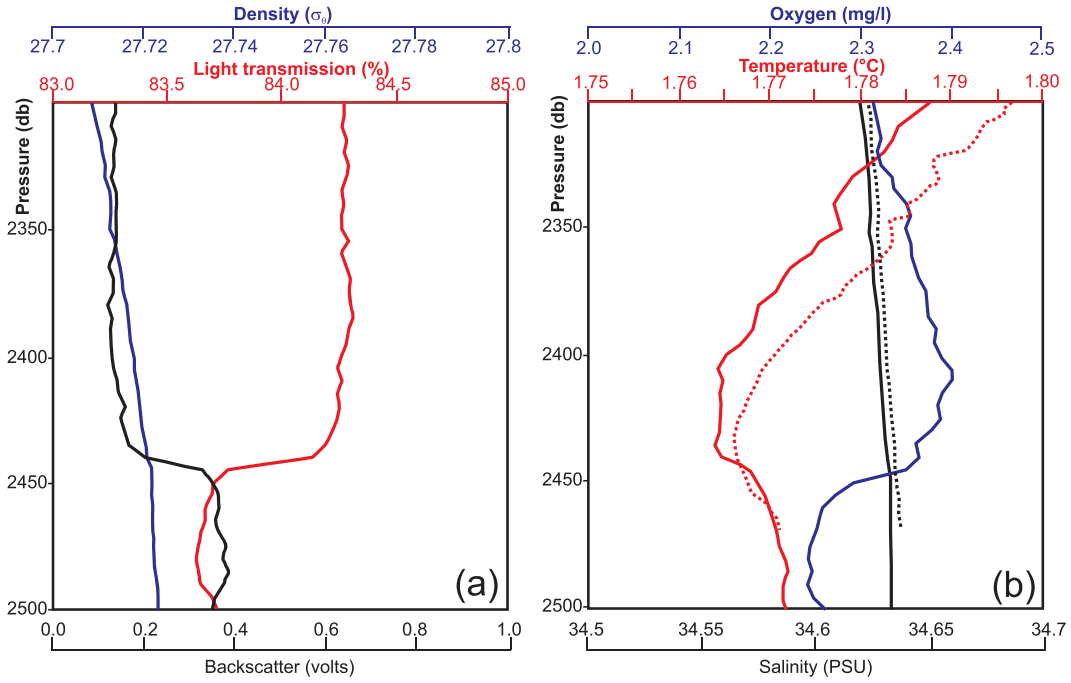


**Figure 11.** CTD data acquired during expeditions carried out aboard R/V *Thomas G. Thompson* (solid lines) and R/V *John P. Tully* (dotted lines) at Maquinna mound in 2001. (a) Potential density ($\sigma_t$), light transmission, and optical backscatter and (b) oxygen, temperature, and salinity. Within the lowermost 50 m, seawater is slightly warmer and lower in oxygen and shows reduced light transmissions and high backscatter values indicative of warm turbid water being expelled at the seafloor.

within the uppermost 300–400 ms TWT to image sediment layers and structural features. A BSR typical of methane hydrate occurrence is observed across the slope region (Figure 13), but overall, data quality is poor, and no continuous BSR pattern was detected. Using the methods described in section 2, the depth

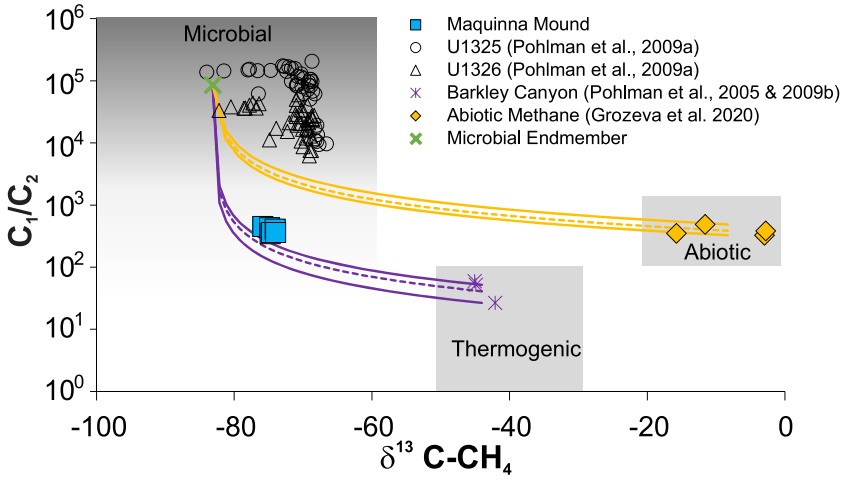


**Figure 12.** Bernard diagram with data from Maquinna Mound compared to data from IODP Expedition 311 Sites U1325 and U1326 (microbial gas), Barkley Canyon (thermogenic gas) and abiotic methane produced by serpentinization. Mixing models between the microbial, thermogenic and abiotic endmembers demonstrate that the Maquinna Mound gas is most likely a mixture of microbial (~80%) and thermogenic (~20%) gas despite geophysical evidence for potential abiotic methane generation by serpentinization in the upper mantle regionally and beneath the mound.

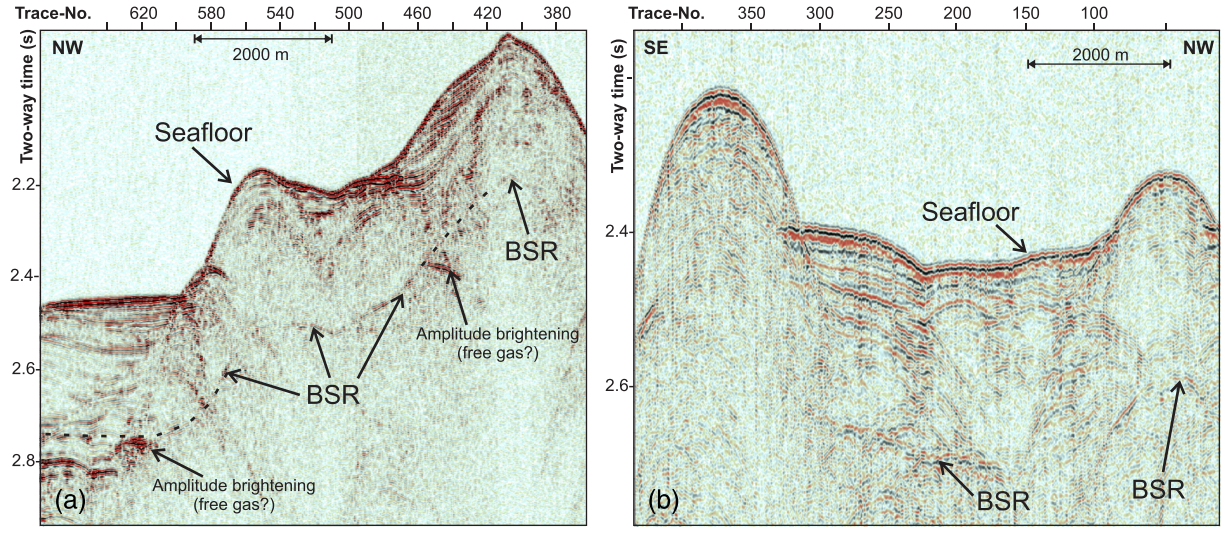


**Figure 13.** Two single-channel seismic sections across the Nootka slope showing the widespread bottom-simulating reflector (BSR) indicative of gas (likely methane) hydrate. For locations, see Figure 1. Vertical exaggeration is 14.

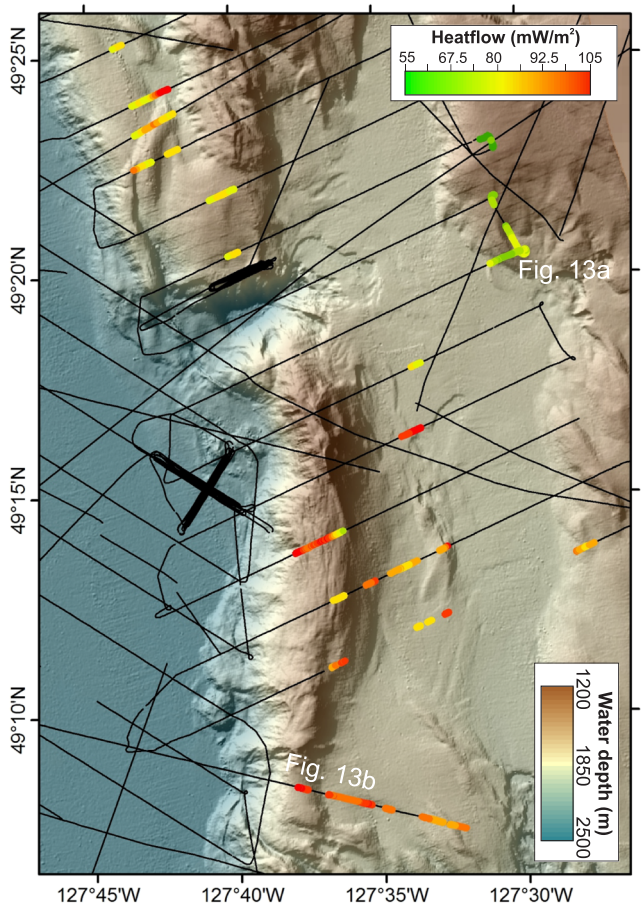


**Figure 14.** Map of BSR-derived heat flow values along the Nootka slope region. Examples of seismic data showing BSRs are given in Figure 13.

of the BSR in this area was converted to heat flow (Figure 14). The thermal effect of topography has been ignored for this initial estimate. Heat flow values vary generally between 55 and 105 mW/m$^2$ across the slope region with a slight geographic trend of decreasing heat flow landwards, as seen further south on the Cascadia margin (Davis et al., 1990; Ganguly et al., 2000).

Gas bubble plumes observed in the water column over topographic expressions during crossings of the slope for OBS deployments and recovery (Riedel, Conway, et al., 2014; Riedel, Côté, Manning, et al., 2014) are additional possible evidence for the occurrence of gas hydrates on the Nootka slope.

As part of the Keck-foundation Nootka study, several ROV dives were carried out along the toe of the slope (see map Figure S3) to locate optimal sites for seismometers and fluid-flow meters (Delaney & Keck Team, 2003; Labonte, 2007; Wilcock et al., 2007). Seafloor videos indicated multiple locations of seafloor fluid seepage sustaining abundant chemosynthetic communities of vestimentiferan tube worms, living vesicomyid clams, dead *Solemya riedi*, and widespread *Beggiatoa* bacterial mats (Figure S4). Venting appears constrained to a fault outcrop seen in the multibeam data along the toe of the first slope ridges as well as along bedding planes of sedimentary layers exposed by seafloor slumping and canyon erosion. Further east into the Nootka slope, evidence for cold vents is from acoustic bubble plumes linked to the tops of ridges (Figure 1), but our observations are sparse. The slope canyon eroded the steep topography and the associated sediment transport created a plunge-pool west of the deformation front. The canyon appears no longer active, as the deformation has created positive topography landward of the plunge pool, and a sharp fault outcrop is visible in the bathymetry (Figure S3, red arrows). However, sediment transport down the canyon must have been prolonged as the sediment fill of the plunge pool is up to 35 m thick (40 ms TWT, 1,600 m/s sediment velocity).

## 4. Interpretation and Discussion

The seismic data acquired in the region of the NFZ provide evidence of abundant fluid and gas flow and shed new light into the processes associated with this transform fault zone.

### 4.1. Bright Spots on the Fault Traces

The bright spots around the two NFZ traces are seen consistently from line to line for up to 20 km along the fault traces but are less than 5 km in extent across the faults themselves (Figure 2c); they appear conformable to the sediment layers (Figures 2c and 5). We suggest two possible explanations for these bright spots: (a) basalt intrusion sills as observed at Middle Valley on the spreading ridge during ODP Leg 139 (Rohr & Gröschel-Becker, 1994; Rohr & Schmidt, 1994) or Escanaba Trough during ODP Leg 169 (Fouquet et al., 1998) and (b) free gas from a deep fluid source that migrated upward into the formations.

The single channel seismic data show that the bright spot reflections across the NFZ traces are semiparallel to the nearly flat seafloor and of opposite polarity (Figure 5). Frequency content of the seismic data is up to 150 Hz providing a vertical resolution of approximately 2–3 m within the uppermost sediment layers. As shown by Rohr and Gröschel-Becker (1994) from synthetic seismogram calculations, stacks of thin sills below the resolution of the seismic data create a complex interference pattern, and the polarity can be difficult to read for sill reflections. Basalt has a much higher acoustic impedance than the surrounding sediments; thus, it would create a top reflection with a polarity identical to the seafloor. Similarly, severe sediment alteration above a sill intrusion causes an increase in both density and velocity, so the polarity of these reflections will remain identical to that of the seafloor (Rohr & Gröschel-Becker, 1994). Alternatively, the polarity of the high-amplitude reflections may indicate free gas that migrated through the faults and was trapped within more permeable sedimentary units. Similar seismic observations of bright spots were made at the Mendocino transform fault by Tréhu et al. (2003) and the strike-slip Hosgri Fault off central California (Kluesner & Brothers, 2016) and interpreted as arising from free gas migrating upward along faults.

Bright spots were observed only along the primary bounding faults, the NNF and the SNF, not the smaller or conjugate faults in between them. The main faults have penetrated down to upper mantle levels, and the smaller faults are confined to the igneous crust (Hutchinson et al., 2019; Figure 2b). This correlation between shallow gas and faulting of upper mantle is intriguing in light of interpretations that serpentinization has been occurring in the upper 0.3–2 km of mantle in the NFZ (Au & Clowes, 1982; Hutchinson et al., 2019; Rohr et al., 2018). It also suggests that something more than simple thermal alteration of organic matter in the sediments is occurring. The latter process would likely generate gas that would migrate along all faults. Occurrence of microearthquakes in upper mantle as opposed to periodic large crustal events has been linked to a higher degree of fracturing and presence of water in the rupture zone (e.g., Froment et al., 2014; Hutchinson et al., 2019; Roland et al., 2012) interpreted that either water in cracks or hydrated alteration minerals were pervasive in and around the rupture zones in upper mantle of the northern NFZ on the basis of low $Vp/Vs$ values. Microseismicity along the Blanco Transform implies that fracturing and hydration have occurred as deep as 13 km below seafloor (Kuna et al., 2019) and has been related to partially serpentinized upper mantle. On the NFZ one might have thought that deposition of sediments in the last few Ma would have prevented fluid flow, but fracture permeability created by frequent ruptures may have allowed fluid flow to occur.

There is a significant difference between seismicity of the NFZ south and north of Conjugate A (Figure S6). There is a high rate of microseismicity north of Conjugate A (Earthquakes Canada, 2020) as was also observed in an OBS deployment (Figure 2), and to the south, a single M6.3 event between 1994 and 2020 was followed by 8 M4 aftershocks. Microseismicity in the north penetrated into the upper mantle (Hutchinson et al., 2019) whereas the 1996 M6.3 in the south and its aftershocks were crustal (Braunmiller & Nábělek, 2002; Ristau et al., 2006). This is similar to variations in seismicity along the Gofar Transform (e.g., McGuire et al., 2012) where M6 events are crustal and microseismicity has been related to fractures carrying water into upper mantle (Froment et al., 2014; Roland et al., 2012). South of Conjugate A, we observe the BSR reflections on the east side of the NFZ but few bright spots along the NNF, although we do not have the same data density as to the north. Presently, a full evaluation of what is occurring south of Conjugate A would rely on the historic earthquake catalog, and fewer reflection

lines. The location of the M6.3 event moved 26 km to the northeast along the NNF when computed using a double-difference technique (Cleveland et al., 2015) which is considered to provide more accurate locations. This uncertainty limits our ability to correlate seismicity patterns to bright spot occurrence in the seismic reflection data. Three-dimensional bending and heavier sediment load closer to the continental slope may also affect stresses on the plate (Rohr et al., 2018).

The fact that basement is elevated below bright spots supports the interpretation proposed in Rohr et al. (2018) that hydration (serpentinization) has expanded the volume of the altered rocks and resulted in isostatic adjustment of the plate assisted by dense faulting. This is visible as uplift of the basement surface (Figures 2d and 5). A definitive interpretation of the nature of these reflections may require detailed seismic velocity analyses (e.g., using multichannel streamer or ocean-bottom seismometers), seafloor compliance, electromagnetic surveys, or deep sea drilling.

Although limited to a maximum depth of seismic imaging of ~0.5 s TWT below seafloor (~ 400 m bsf), there seems to be a truncation of bright spots slightly east of the two seafloor mounds (i.e., ~15 km west of the deformation front; Figure 2c). Alternatively, bright spots may be simply occurring deeper than our observation limit; yet this truncation (or possible deepening) of the depth to which free gas may be able to migrate is an interesting observation in itself. Overall, basement is gradually deepening toward the toe of the slope, and sediment thickness is increasing due to much higher sedimentation rates near the trench (see, e.g., Figure 2d). Fault permeability may therefore be reduced, and free gas can no longer migrate as easily upward as further west of the toe of the slope. Another complexity may arise from interactions with the slope itself and associated changes in the horizontal stress regime, as, for example, suggested by Han et al. (2016) for a region ~10–15 km west of the Cascadia deformation front off Oregon and Washington.

### 4.2. BSR-Like Events and Faulting on the Abyssal Plain

The high-amplitude reflections further southeast of the NFZ with their prominent crosscutting nature may also be free gas related. The polarity of the shallowest bright spots is clearly opposite to that of the seafloor. Here, an additional explanation of gas hydrate formation may explain the unique crosscutting behavior. Basaltic intrusions would not likely result in a crosscutting reflection pattern nor in enhanced underlying amplitudes. Amplitudes should be diminished from transmission loss at the high-impedance contrasts of the basaltic sills. If we attribute these crosscutting reflections to a phase boundary of gas hydrates above and free gas underneath, then the nonbottom simulating behavior of the reflections requires explanation. The reflections are over fault systems (Figure 6) that might facilitate upward migration of warmer fluids that mix and diffuse into the surrounding sediments. The sediment may in turn cool away from the fault trace causing a deepening of the BSR-like reflections with distance from the fault trace. The irregular thermal regime may give an irregular hydrate stability boundary. The maximum distance of the high-amplitude reflections from the fault is likely the result of a combination of the limit in driving force as well as permeability of the sediments. Treating these reflections as gas hydrate related, then the depth of the reflection below seafloor may be used to estimate heat flow values under the assumption of a given pore fluid salinity (34 ppt) and gas composition. Following the methods described above, the depth of the BSR-like event shown in Figure 6a would require an average heat flow value of ~450 $mW/m^2$ for a pure methane system. Similarly, the example in Figure 6b results in an average heat flow value of 250 $mW/m^2$. Both these values are higher than most of the probe measurements reported by Davis and Lister (1977a, 1977b) about 20–40 km to the west. The heat flow data from a 1971 survey (Davis & Lister, 1977a, 1977b) are highly variable, from ~150 to ~300 $mW/m^2$ along a 50 km N-S transect (compare to Figure 1). This was interpreted to indicate active hydrothermal flow in the sediments and upper igneous crust. Adding higher hydrocarbons than methane to the gas compositions (or $CO_2$) would result in even higher heat flow values for the same depths of these reflections. Only higher salt concentrations within the pore fluids would reduce heat flow for identical subseafloor depths of the reflections. One potential source for such excess salt could be found associated with the serpentinization reactions at depth as described, for example, by Scribano et al. (2017), which could be leached and brought to the surface by hydrothermal venting. Active faulting can reach into the upper mantle as shown from the seismicity study by Hutchinson et al. (2019) and is likely to partake in, if not, facilitate hydrothermal circulation. Serpentinization of the top 0.3–2 km of upper mantle was proposed to be possible by Au and Clowes (1982), Hutchinson et al. (2019), and Rohr et al. (2018). If these BSR-like reflections are indeed gas hydrate related and if the source of methane and excess salt is produced at depths from

serpentinization reactions (as also postulated at other gas hydrate provinces, such as off Svalbard, Johnson et al., 2015), this could be tested by coring (or deep drilling) and linked geo-chemical analyses. However, no work to test for mantle origin of fluids has been carried out for these sites, and thus, these aspects of the cause for the BSR-like reflections remain speculative.

This fault zone is a prime location to test for geochemical signatures of active hydration of upper mantle. Crustal structure was initially fairly uniform having formed at a single spreading center, and it is presently being ruptured in earthquakes that occur down to upper mantle (Hutchinson et al., 2019). The upper mantle has low *Vp*/*Vs* ratios, which require water in the mantle either in pervasive cracks or to hydrate the mantle or most likely, in some combination of the two compositions (Hutchinson et al., 2019). There is abundant evidence of fluid flow and evidence of the isostatic effects of extensive hydration on the upper boundary of igneous crust (Rohr et al., 2018).

### 4.3. Gas Hydrate Occurrences on Slope

On the other hand, there is ample evidence for gas hydrate along the Nootka slope from BSRs, cold vents with chemosynthetic communities, widespread carbonate formations, and free gas venting. As the oceanic plates (Explorer to the North and Juan de Fuca to the South) are both subducted underneath Vancouver Island, a short (~36 km) and steep (~4°) accretionary prism is formed along the Nootka slope. This process is accompanied by rapid tectonic compression and fluid expulsion (Hyndman & Davis, 1992; Riedel, Collett, et al., 2010), giving rise to the abundant occurrence of gas hydrates, cold vents, and gas emissions. Heat flow values derived from the BSR depth for a pure methane system at the Nootka slope are on average ~80 mW/m$^2$ with a range from ~55–105 mW/m$^2$ (Figure 14) but overall decreasing landward. The values and overall reducing landward trend are similar to those of the northern Cascadia accretionary prism (e.g., Ganguly et al., 2000; He et al., 2007; Hyndman et al., 1993; Riedel, Tréhu, et al., 2010). These heat flow values are an important input to thermal modeling of subduction to estimate thermal control of great earthquake shaking and tsunamis. Previous work on the Explorer plate by Gao et al. (2017) had no heat flow constraints in the marine section of their model.

### 4.4. Seafloor Mounds

The two seafloor mounds (Haggis and Maquinna) (Figure 7) are rather unusual structures and the only ones of their type found along the Cascadia margin. Riedel et al. (2001) originally described these structures as active mud volcanoes. They are similar to mud volcanoes in other tectonic settings and more specifically where sediment covered strike-slip faulting promotes rise of crustal-derived hydrothermal fluids (e.g., Gulf of Cadiz abyssal plain: Hensen et al., 2007, 2015). The NFZ mounds display prominent doming of the sediment structures (Figures 8 and 10), semicircular moats, and possible mud flows inside the moats themselves; however, the two mounds lack some characteristics seen at other deep water mud volcanoes, such as interfingering of mud flows with surrounding sediments, so-called Christmas-tree structures (e.g., Perez-Garcia et al., 2011; Praeg et al., 2009), or the formation of larger outflow sheets or pathways (e.g., Bohrmann et al., 2003; Paull et al., 2008, 2015). Deep beneath the two features (400–800 mbsf), bright and steeply dipping reflections are seen with sediments above appearing to partially mimic the topography of these structures (Figure 15). Upward bending of the layers is progressively reduced toward the seafloor. Deformation is overall smaller at Haggis, where only minor residual upward bending of the layers remains above the bright spot. The shape of the bright spot underneath Haggis is still somewhat mimicked by the layer indicated by the blue dotted line in Figure 15; yet this is already diminished only ~50 ms (TWT) shallower (cyan-colored dotted line in Figure 15).

These mounds are similar to mound-like features investigated at Middle Valley as well as Escanaba Trough, which were described as sedimentary plugs uplifted over basaltic intrusions 500–600 m below the seafloor (Denlinger & Holmes, 1994). The mound in Middle Valley occurs over igneous crust less than 100 ka old and is just 5 km from the southernmost tip of the NNF (see Figures 3b, 6a, and 7 in Davis & Villinger, 1992). Multiple mounds were imaged along the spreading axis of Escanaba Trough (Davis & Becker, 1994); they were often surrounded by high-temperature hydrothermal deposits (Denlinger & Holmes, 1994).

The CTD measurements at Maquinna mound show that warm fluids are expelled from the center of the mound. These fluids sustain some chemosynthetic communities as seen by the white galatheid crabs that

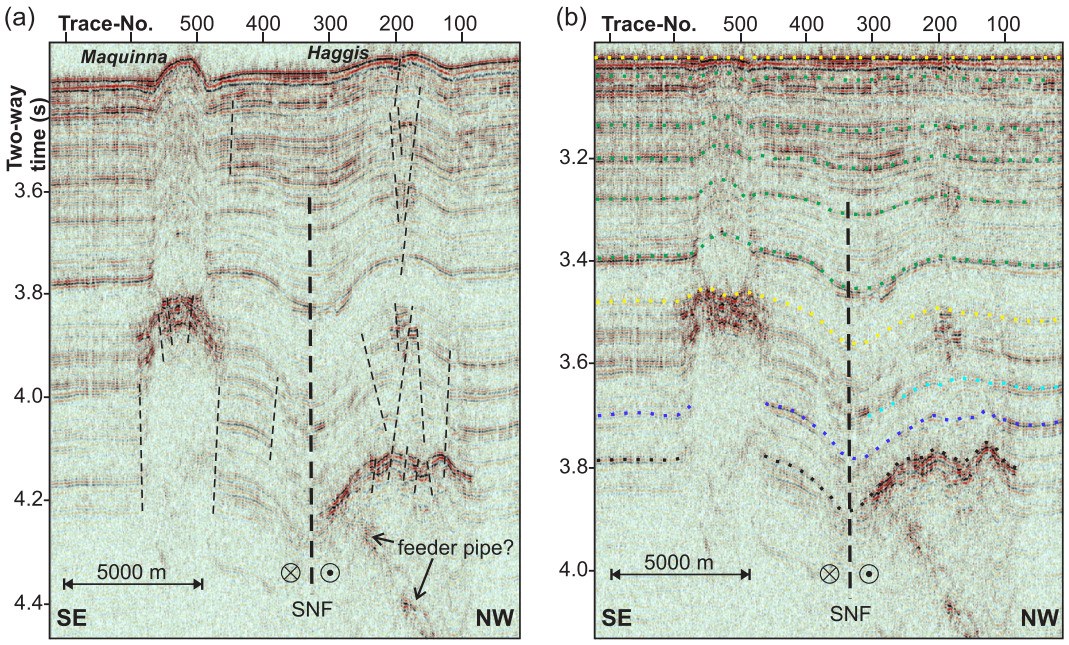


**Figure 15.** Seismic line connecting Haggis and Maquinna mound with original topography shown in (a) and flattened to seafloor shown in (b). Sediment layers above the bright spot are deflected upward (green dotted lines) relative to the area outside the mounds. Several faults are seen at Haggis, along which small bright spots have developed toward the seafloor. Faulting cannot be mapped with confidence right underneath Maquinna due to the overall steep topography. The sediment layers around the southern Nootka Fault trace (SNF) are depressed in the typical V-shape pattern of a strike-slip fault. Vertical exaggeration is 22.

are normally associated with hydrothermal systems, as well as clams that indicate active fluid expulsion at the seafloor (Figures S2 and S4).

The sediment cores collected on and off the mound allow for some interpretation of deeper processes. In Piston Core C17 (Figure S1), the occurrence of methane and its associated SMTZ within 3 m of the seafloor suggests active transport of methane from greater depth. The upper 3 m bsf at Maquinna is nearly constant in chloride and sulfate concentrations, underlain by sediments showing high methane values and the occurrence of some ethane, yielding relatively low $C_1/C_2$ ratios. The occurrence of ethane at Maquinna may be a result of a contribution of thermogenic gases or, perhaps, enhanced microbial ethane production stimulated by the warmer sediment environment as suggested by the expulsion of warm fluids at the seafloor as seen in the CTD data. The single background core taken ~6 km SE of Maquinna shows more typical deep water marine profiles of all pore water constituents with no significant methane (<0.008 mM $CH_4$) or measured ethane. The depth of sulfate depletion where an SMTZ might be expected is extrapolated to ~10 m bsf assuming a linear sulfate profile below the depth of core recovery.

The uplifted basement rocks beneath the bright spots at Haggis and Maquinna mounds are consistent with a volume expansion of mantle-derived peridotite having undergone hydration such as abiotic methane producing serpentinization (Johnson et al., 2015; Rohr et al., 2018). The $\delta^{13}C$ of methane from fluid inclusions within peridotite host rocks from the Mid-Cayman rise range from −15.8‰ to −2.8‰ (Grozeva et al., 2020). These values are typical for mafic and ultramafic systems where serpentinization is active (McDermott et al., 2015), or gas generated by this process has been captured within fluid inclusions (Grozeva et al., 2020). To evaluate if the methane present within the shallow sediments (<10 m bsf) of Maquinna Mound contains an abiotic component, the mixing models between a known $^{13}C$-depleted microbial methane endmember from the northern Cascadia margin (Pohlman, Kaneko, et al., 2009), a thermogenic endmember from the Barkley Canyon hydrocarbon seep (Pohlman, Bauer, et al., 2009; Pohlman et al., 2005), and peridotite-hosted abiotic methane from the Mid-Cayman Rise (Grozeva et al., 2020) were constructed (Figure 12). The data from Maquinna Mound most closely aligns with the mixing model between the

microbial and thermogenic endmembers. Although abiotic methane $\delta^{13}C$ values are occasionally as low as −50‰ (Milkov & Etiope, 2018), which resembles the thermogenic endmember from Barkley Canyon, production of abiotic methane involving ultramafic rocks at NFZ is more likely to have similar $\delta^{13}C$ values as those from other ultramafic-influenced systems like the Mid-Cayman Rise (Grozeva et al., 2020). Therefore, we conclude that methane within the shallow sediments beneath Maquinna Mound is primarily microbial in origin with a slight (~20%) contribution from a thermogenic source, which is likely related to the thermal alteration of sediment organic matter created by the basaltic intrusion event.

All these observations combined with similarities to the mounds in Middle Valley and Escanaba Trough (Davis & Villinger, 1992) favor the interpretation of basalt intrusions as the source of bright reflectors under Maquinna and Haggis mounds. The mounds in Escanaba Trough formed in an active spreading center, so the presence of basalt in sediments is easily explained. In Middle Valley, the sediment mound formed in the now extinct half graben of the spreading center at the southern tip of the NNF, which transects the eastern side of the Valley. Stress concentration at fault tips results in many vent sites occurring close to the tips (Curewitz & Karson, 1997); this setting could allow residual magma beneath the extinct spreading center to be brought up into the sediments. The origin of basalt further north in the NFZ in a transform fault that cuts young oceanic plate is not so obvious, yet local regions of extension surely exist. As expected from the broad nature of the NFZ, the tectonic regime includes areas of both local transpression and transtension. Evolution of extensional minibasins between Riedel shear faults may open pathways for deep-rooted fluids including basaltic melt to move vertically upward. Typical S-shaped en échelon fault segments develop along the fault traces on the abyssal plain and pull-apart minibasins (Figure 4) open between the segments. The shape and orientation of the en échelon fault segments are consistent with initiation of a left-lateral strike-slip fault and evolution of segments in left stepovers and Riedel shears (Rohr et al., 2018).

The mounds described here are near the northern tip of the surficial expression of the SNF (Figure 2 in Rohr et al., 2018), but reflection sections and seismicity up to 20 km bsf indicate that this fault continues northward at deeper levels. Historically, this location may have been the northern terminus of the SNF and similar to Middle Valley tapped a deep source of melt. The morphologic similarities to the sediment mounds observed in spreading centers are too great to ignore, even though the origin of the basalt is not obvious.

The sediment layers above the high-amplitude zone are subparallel at both NFZ mound structures. This can be explained by (i) sediment layers being deposited gradually above paleo-topography (drape), (ii) upward bending from fluid/gas pressure created by the initial emplacement of an intrusion or gas pocket, or (iii) mechanical displacement of sediment as result of the emplacement of an intrusion. We do not favor the explanation of drape, as there are no clear sediment onlap structures and this is a region of common turbidite flows (Davis & Hyndman, 1989). The regional basement topography shows much higher elevation changes over similar short distances as the mounds, and yet regional basement is covered by the same thick sediment sequence with no seafloor expression of the original basement topography (Figure 2d). If fluid overpressure is due to a gas or basalt intrusion, then the bright spots mark the seal, that is, maximum height up to which the fluids have migrated from greater depth. The amount of doming (minimum 30 m elevation above the abyssal plain) is then a measure of the overpressure underneath the bright spots. No gas discharge was detected during numerous crossings of these mounds. However, warm fluids were detected by CTD casts supporting the interpretation of emplacement of basalt at depth, liberating warm fluids that rise to the surface and sustain the chemosynthetic communities at the seafloor. The third possible explanation that the doming above the bright spots is the result of the emplacement of a body of basalt requires that deformation seen above the bright spot is different from below. The elevation of the mounds above the abyssal plain seafloor would in part be a representation of the volume of anomalous material (i.e., basalt) intruded at depth.

We infer from all the combined data that the two mounds are possibly the result of basalt intrusions at depth, but their intrusion times appear different. Maquinna mound is at an active phase with sustained overpressure that results in the upward doming of overlying sediment layers and venting at the seafloor. In contrast, the intrusion at Haggis mound no longer sustains the same level of overpressure as at Maquinna, and the system appears deflated. This is depicted in the model of mound formation in Figure 16.

At the initial stage (Figure 16a), local extension along the NFZ (which is cutting through the sedimentary layers and basement) allows melt/fluids to rise from greater depth leading to the emplacement of a small intrusion. This results in initial mechanical upward push of overlying strata (similar to the model

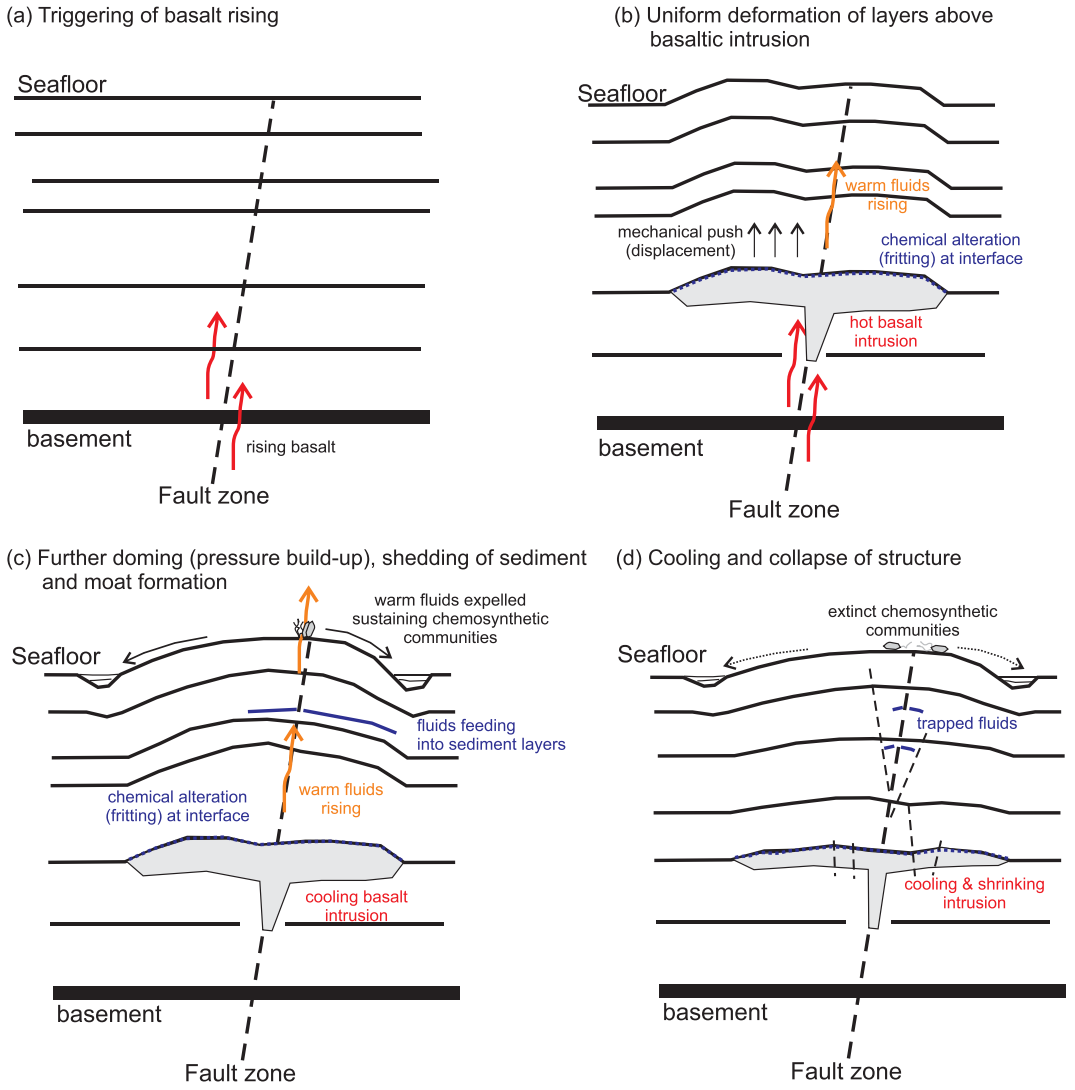


**Figure 16.** Model for evolution of seafloor mounds Haggis and Maquinna. (a) Initial stage of Nootka fault cutting through sedimentary layers and basement, and rising melt from greater depth; (b) emplacement of intrusion with associated initial mechanical upward push of overlying strata; (c) intrusion reacts with sediments and pore fluids and heat generates fluid flow. (d) As an intrusion cools over time, it will shrink, resulting in subsidence and collapse (for details, see text).

proposed by Denlinger & Holmes, 1994; Figure 16b). The heat from the intrusion generates flow of fluids within the sediments, and the intrusion reacts chemically with the sediments, releasing secondary fluids that migrate further upward. These fluids in part can also leak horizontally into more permeable sedimentary layers, thereby forming conformable bright spots. Some fluids are ultimately released at the seafloor where they sustain chemosynthetic communities. Microbial methane produced in situ is transported toward seafloor. Secondary migration of fluids can mobilize sediments and create overpressure, pushing the mound further upward. The sustained height of the mound above the abyssal plain results in formation of a moat due to deformation from the mound's own weight, where subsequently mud flows and other sediments shed off the mound are collected (Figure 16c). As the intrusion cools over time, it will shrink somewhat, resulting in subsidence and collapse, and overpressure is not maintained as fluid circulation is diminished. Sediment layering then subsides and may again become seafloor parallel (Figure 16d). Maquinna mound appears still at an active phase with sustained overpressure and fluid flow, whereas Haggis seems to be at the end of the mound inflation cycle.

Studies of hydrogeology of Juan de Fuca plate have shown that a blanket of a few hundred meters of hemipelagic mud is sufficient to seal the igneous crust from fluid flow (Davis & Villinger, 1992; Underwood et al., 2005). Interpretations by Denlinger and Holmes (1994) as well as Loher et al. (2018) show that ring faults are important conduits bringing fluids to the seafloor. Volcanic features are not unusual along transform plate boundaries because faults rarely follow exact small circles relative to the pole of rotation and zones of extension and compression are the result. Changes in the direction of motion also set up zones of extension and compression. Fornari et al. (1989) and Pockalny et al. (1997) described the response of a transform plate boundary to changes in plate motion that put the entire transform into extension: faulted basins (extensional relays) in transforms become volcanically active (leaky) and with continued displacement evolve into intratransform spreading centers. The effects of these changes can be seen along the length of the plate boundary, which in the case of the Siqueiros transform is approximately 100 km long. The NFZ displays kilometer-scale extensional zones and in the recent past small compressional folds in the southern portion of the fault zone (Rohr et al., 2018). The dominant focal mechanisms in microseismicity monitored by OBSs (Hutchinson et al., 2019) are left-lateral strike slip with lesser numbers of thrust and normal mechanisms observed throughout (Figure S7). The relative plate motion of the Explorer plate is not well determined because of a lack of well-defined magnetic lineations, so it is not clear if these small structures along the NFZ are created by regional stresses or are simply local.

## 5. Summary and Conclusions

A wide range of data, especially seafloor multibeam swath imagery, single-channel seismic reflection, and 3.5 kHz subbottom profiler data have allowed detailed mapping of the two traces of the NFZ, the boundary between the Juan de Fuca and Explorer plate, along with associated sedimentary deformation and fluid expulsion processes. In the southern fault zone broad bright spots are similar to BSR's and may indicate the presence of methane hydrate. In the northern fault zone, long shallow stacked bright spots are concentrated above the main fault traces; these also are likely to be caused by gas. In addition, two sedimentary mounds are underlain by complexes of bright spots; their similarity to mounds above basalt sills in an active and an extinct spreading center suggests that there may also have been a small amount of intrusive activity along the NFZ.

The sediment-hosted bright spots along the main traces of the NFZ, coupled with elevated basement, occur in a limited range: from ~38 km northeast of the initiation of the NFZ at Middle Valley up to the seafloor mounds. In the same locations microearthquakes occurring in upper mantle and low $Vp/Vs$ ratios have been interpreted to indicate the presence of water in fractures or talc (Hutchinson et al., 2019). Similarly, microseismicity in mantle and low $Vp$ values have been interpreted to indicate the presence of water in fractures on the Gofar transform (McGuire et al., 2012). We suggest that at the NFZ repeated ruptures create fracture permeability allowing fluid flow from the seafloor into upper mantle some of which is trapped in permeable layers in shallow sediments.

The bright spots under the mounds are similar to those studied at the Escanaba Trough and Middle Valley. The prominent donut-shaped seafloor mound Maquinna is associated with a thermal anomaly in near-bottom water, and there are observations of galatheid crabs typically associated with hydrothermal vents. The presence of relatively high ethane at Maquinna in comparison to the abyssal plain core site further indicates the ascension of deep-sourced fluids at the mound, which may be related to thermal convection driven by the emplacement of a basalt intrusion beneath the mound. The deep bright spots seen in seismic data beneath both mounds are concluded to be caused by the strong impedance contrast between basalt and sediments. This intrusion is a heat source that results in hydrothermally driven upward migration of fluids and gas that maintain the positive relief features despite the regional high sedimentation rates. Frequent earthquakes and repeated fracture of the sediments and underlying crust have undoubtedly facilitated fluid flow in the fault zone.

The bright spots in abyssal plain sediments observed here are unusual. Although gas in the sediments could arise from processes in the sediments alone, melt to form basalt intrusions must arise from much deeper levels. In addition, hydration occurring in the lower crust to upper mantle has been inferred from uplift of basement in the fault zone (Rohr et al., 2018) and low $Vp/Vs$ ratios in upper mantle (Hutchinson et al., 2019). These processes may further affect the composition of fluids in the sediments.

Broad bright spots seen in the southern portion of the NFZ show characteristics of typical methane hydrate related BSRs. Although not all fully bottom simulating, these bright spots are of opposite polarity to the seafloor reflection, crosscut sedimentary layers, and are associated with gas brightening underneath. If these bright spots are linked with methane hydrate, the depths of the reflections suggest local heat flow of 250–450 mW/m$^2$.

In contrast, widespread gas-hydrate associated BSRs on the Nootka slope are interpreted to result from tectonic compression of the sediments near and in the accretionary prism and upward fluid advection. Cold vents with chemosynthetic communities and gas plumes across the slope are further evidence for fluid advection. BSR-derived heat flow estimates for the Nootka slope region are on average 80 mW/m$^2$, which are as expected for the plate age and geological setting and are similar to values from further south on the accretionary prism (e.g., Ganguly et al., 2000). The estimated uncertainty is at least ~20%.

Oceanic transforms are globally pervasive tectonic features that are conduits for chemical exchanges between mantle, overlying crust, and seawater, yet they remain underexplored and mechanisms linking fluid flow, seismicity, and seafloor ecosystems are poorly understood (Hensen et al., 2015; McGuire, 2019; Prigent et al., 2020). The NFZ is a relatively young ridge-trench transform that was initiated in an oceanic plate formed in a normal oceanic spreading center (Rohr et al., 2018); its structure was initially simpler than ridge-ridge transforms, which by definition form at the far end of the spreading segment with likely smaller magma input, greater thermal contrast across the fault, and during active shearing. The abundant and diverse examples documented here of fluid flow coincident with seismicity (Hutchinson et al., 2019) make the NFZ a good location to study these processes in part because sediments can trap the fluids. The NFZ can also provide an example of how subduction of a hydrated fault zone affects regional seismicity and potential megathrust activity.

Future work in the region should include additional geophysical surveying, especially multichannel seismic reflection data or the use of OBSs to determine the local velocity structure and to determine the nature of the bright spots along the NFZ by seafloor compliance or controlled-source electromagnetic imaging. Additional coring at faults and seafloor mounds to decipher the source of methane would be useful with associated isotopic analyses of pore fluids, head space or void gases. Coring around minibasins and the moats of the mounds would also help the interpretation of ages of these features, rates of motion along faults, and/or episodes of mud flows from the seafloor mounds.

## Data Availability Statement

Some of the Canadian seismic reflection data used in this analysis are curated by Natural Resources Canada and are available online (at the following site: http://ftp.maps.canada.ca/pub/nrcan_rncan/raster/marine_geoscience/Seismic_Reflection_Scanned/NRCan_Seismic_Reflection_Scanned.kmz). Additional data can be requested from scientists at the Geological Survey of Canada (curator Michelle Côté, michelle.cote@canada.ca) or through the Open Government Portal (https://open.canada.ca/data/en/dataset/b9400595-b5b6-4a76-b34e-b437178adb45). Heat probe data were previously published, and the original data including navigation can be accessed in the paper by Davis and Lister (1977a). Bottom-video data are maintained through the Monterey Bay Aquarium Research Institute (www.mbari.org). Access to video data can be accessed through direct requests to the data repository team at MBARI (for details see https://www.mbari.org/products/data-repository/). We herewith also thank Nancy Jacobsen Stout from MBARI for accessing videos data and associated species identifications at Maquinna mound. Global multiresolution topography (GMRT, Ryan et al., 2009) was used to generate topographic and bathymetric maps using ArcGIS V.10.2. Data are available for map-generation online (at https://www.gmrt.org/GMRTMapTool/)

## Conflict of Interest

There are no real or perceived financial conflict of interest for any author.

**Acknowledgments**

This study represents data from numerous cruises acquired over more than two decades. We would like to thank all the scientific personnel and technical staff involved in data acquisition, processing of samples, and making observations during the ROV dives, as well as the crews and captains of the various research vessels involved. This is contribution #5877 from the University of Maryland Center for Environmental Science. This is NRCan contribution number / Numéro de contribution de RNCan: 20200324. Disclaimer: Any use of trade names is for descriptive purposes and does not imply endorsement by the U.S. government.

## References

Au, D., & Clowes, R. M. (1982). Crustal structure from an OBS survey of the Nootka fault zone off western Canada. *Geophysical Journal of the Royal Astronomical Society*, *68*(1), 27–47. https://doi.org/10.1111/j.1365-246X.1982.tb06960.x

Au, D., & Clowes, R. M. (1984). Shear-wave velocity structure of the oceanic lithosphere from ocean bottom seismometer studies. *Geophysical Journal of the Royal Astronomical Society*, *77*(1), 105–123. https://doi.org/10.1111/j.1365-246X.1984.tb01927.x

Bernard, B. B., Brooks, J. M., & Sackett, W. M. (1978). Light-hydrocarbons in recent Texas continental-shelf and slope sediments. *Journal of Geophysical Research*, *83*(C8), 4053–4061. https://doi.org/10.1029/JC083iC08p04053

Boetius, A., Ravenschlag, K., Schubert, C. J., Rickert, D., Widdel, F., Gieseke, A., et al. (2000). A marine microbial consortium apparently mediating anaerobic oxidation of methane. *Nature*, *407*(6804), 623–626. https://doi.org/10.1038/35036572

Bohrmann, G., Ivanov, M., Foucher, J. P., Spieß, V., Bialas, J., Weinrebe, W. R., et al. (2003). Mud volcanoes and gas hydrates in the Black Sea—New data from Dvurechenskii and Odessa mud volcanoes. *Geo-Marine Letters*, *23*(3–4), 239–249. https://doi.org/10.1007/s00367-003-0157-7

Botros, M., & Johnson, H. P. (1988). Tectonic evolution of the Explorer-northern Juan de Fuca region from 8 Ma to the present. *Journal of Geophysical Research*, *93*(B9), 10,421–10,437. https://doi.org/10.1029/JB093iB09p10421

Braunmiller, J., & Nábělek, J. (2002). Seismotectonics of the Explorer region. *Journal of Geophysical Research*, *107*(B10), 2208. https://doi.org/10.1029/2001JB000220

Cassidy, J. F., Ellis, R. M., Karavas, C., & Rogers, G. C. (1998). The northern limit of the subducted Juan de Fuca plate. *Journal of Geophysical Research*, *103*(B11), 26,949–26,961. https://doi.org/10.1029/98JB02140

Chuang, P. C., Yang, T. F., Wallmann, K., Matsumoto, R., Hu, C. Y., Chen, H. W., et al. (2019). Carbon isotope exchange during anaerobic oxidation of methane (AOM) in sediments of the northeastern South China Sea. *Geochimica et Cosmochimica Acta*, *246*, 138–155. https://doi.org/10.1016/j.gca.2018.11.003

Cleveland, K. M., VanDeMark, T. F., & Ammon, J. C. (2015). Precise relative locations for earthquakes in the northeast Pacific region. *Journal of Geophysical Research*, *120*(10), 6960–6976. https://doi.org/10.1002/2015JB012161

Curewitz, D., & Karson, J. A. (1997). Structural settings of hydrothermal outflow: Fracture permeability maintained by fault propagation and interaction. *Journal of Volcanology and Geothermal Research*, *79*(3-4), 149–168. https://doi.org/10.1016/S0377-0273(97)00027-9

Davis, E. E., & Becker, K. (1994). Thermal and tectonic structure of the Escanaba Trough: New heat-flow measurements and seismic-reflection profiles. In J. L. Morton, R. A. Zierenberg, & C. A. Reiss (Eds.), *Geologic, hydrothermal, and biologic studies at Escanaba Trough, Gorda Ridge, offshore northern California*, *U.S. Geological Survey Bulletin* (Vol. 2022, pp. 45–64). Denver, CO: U.S. Department of the Interior.

Davis, E. E., & Hyndman, R. D. (1989). Accretion and recent deformation of sediments along the northern Cascadia subduction zone. *Geological Society of America Bulletin*, *101*(11), 1465–1480. https://doi.org/10.1130/0016-7606(1989)101<1465:AARDOS>2.3.CO;2

Davis, E. E., Hyndman, R. D., & Villinger, H. (1990). Rates of fluid expulsion across the northern Cascadia accretionary prism: Constraints from new heat flow and multichannel seismic reflection data. *Journal of Geophysical Research*, *95*(B6), 8869–8889. https://doi.org/10.1029/JB095iB06p08869

Davis, E. E., & Lister, C. R. B. (1977a). Heat flow measured over the Juan de Fuca Ridge: Evidence for widespread hydrothermal circulation in a highly heat transportive crust. *Journal of Geophysical Research*, *82*(30), 4845–4860. https://doi.org/10.1029/JB082i030p04845

Davis, E. E., & Lister, C. R. B. (1977b). Tectonic structures on the northern Juan de Fuca ridge. *Geological Society of America Bulletin*, *88*, 346–363. 1977

Davis, E. E., & Villinger, H. (1992). Tectonic and thermal structure of the Middle Valley sedimented rift, northern Juan de Fuca Ridge. In E. E. Davis, M. J. Mottl, A. T. Fisher, et al. (Eds.), *Proceeding of Ocean Drilling Program*, *Initial Reports* (Vol. 139, pp. 9–41). College Station, TX: Ocean Drilling Program. https://doi.org/10.2973/odp.proc.ir.139.102.1992

Delaney, J. R., & Keck Team (2003). *Plate tectonic modulation of microbial productivity in the deep ocean—A Keck-supported Proto-NEPTUNE experiment,* Paper presented at American Geophysical Union Fall Meeting 2003.

Denlinger, R. P., & Holmes, M. L. (1994). A thermal and mechanical model for sediment hills and associated sulfide deposits along the Escanaba Trough. In J. L. Morton, R. A. Zierenberg, & C. A. Reiss (Eds.), *Geologic, hydrothermal, and biologic studies at Escanaba Trough, Gorda Ridge, offshore northern California*, *U.S. Geological Survey Bulletin* (Vol. 2022, pp. 65–75). Denver, CO: U.S. Department of the Interior.

Dooley, T. P., & Schreurs, G. (2012). Analogue modelling of intraplate strike-slip tectonics: A review and new experimental results. *Tectonophysics*, *574-575*, 1–71. https://doi.org/10.1016/j.tecto.2012.05.030

Dziak, R. P. (2006). Explorer deformation zone: Evidence of a large shear zone and reorganization of the Pacific-Juan de Fuca-North American triple junction. *Geology*, *34*(3), 213–216. https://doi.org/10.1130/G22164.1

Earthquakes Canada (2020). *GSC, earthquake search* (on-line bulletin). Natural Resources Canada. Retrieved from http://earthquakescanada.nrcan.gc.ca/stndon/NEDB-BNDS/bulletin-en.php

Englezos, P., & Bishnoi, P. R. (1988). Prediction of gas hydrate formation in aqueous solutions. *American Institute of Chemical Engineers*, *34*(10), 1718–1721. https://doi.org/10.1002/aic.690341017

Fornari, D. J., Gallo, D. G., Edwards, M. H., Madsen, J. A., Perfit, M. R., & Shor, A. N. (1989). Structure and topography of the Siqueiros transform fault system: Evidence for the development of intra-transform spreading centres. *Marine Geophysical Researches*, *11*(4), 263–299. https://doi.org/10.1007/BF00282579

Fouquet, Y., Zierenberg, R. A., Miller, D. J., Bahr, J. M., Baker, P. A., Bjerkgarden, T., et al. (1998). *Proceedings Ocean Drilling Program, Initial Reports* (Vol. 169). College Station, TX: Ocean Drilling Program. https://doi.org/10.2973/odp.proc.ir.169.101.1998

Froment, B., McGuire, J. J., van der Hilst, R. D., Gouedard, P., Roland, E. C., Zhang, H., & Collins, J. A. (2014). Imaging along-strike variations in mechanical properties of the Gofar transform fault, East Pacific Rise. *Journal of Geophysical Research: Solid Earth*, *119*, 7175–7194. https://doi.org/10.1002/2014JB011270

Ganguly, N., Spence, G. D., Chapman, N. R., & Hyndman, R. D. (2000). Heat flow variations from bottom simulating reflectors on the Cascadia margin. *Marine Geology*, *164*(1-2), 53–68. https://doi.org/10.1016/S0025-3227(99)00126-7

Gao, D., Wang, K., Davis, E. E., Jiang, Y., Insua, T. L., & He, J. (2017). Thermal state of the Explorer segment of the Cascadia subduction zone: Implications for seismic and tsunami hazards. *Geochemistry, Geophysics, Geosystems*, *18*, 1569–1579. https://doi.org/10.1002/2017GC006838

Gao, D., Wang, K., Insua, T. L., Sypus, M., Riedel, M., & Sun, T. (2018). Defining megathrust tsunami source scenarios for northernmost Cascadia. *Natural Hazards*, *94*(1), 445–469. https://doi.org/10.1007/s11069-018-3397-6

Govers, R., & Meijer, P. T. (2001). On the dynamics of the Juan de Fuca plate, earth and plant. *Science Letters*, *189*, 115–131.

Grozeva, N. G., Klein, F., Seewald, J. S., & Sylva, S. P. (2020). Chemical and isotopic analyses of hydrocarbon-bearing fluid inclusions in olivine-rich rocks. *Philosophical Transactions of the Royal Society A*, *378*, 20180431. https://doi.org/10.1098/rsta.2018.0431

Han, S., Carbotte, S. M., Canales, J. P., Nedimovic, M. R., Carton, H., Gibson, J. C., & Horning, G. W. (2016). Seismic reflection imaging of the Juan de Fuca plate from ridge to trench: New constraints on the distribution of faulting and evolution of the crust prior to subduction. *Journal of Geophysical Research: Solid Earth*, *121*, 1849–1872. https://doi.org/10.1002/2015JB012416

Hasselgren, E. O., & Clowes, R. M. (1995). Crustal structure of northern Juan de Fuca plate from multichannel reflection data. *Journal of Geophysical Research*, *100*(B4), 6469–6486. https://doi.org/10.1029/94JB02941

He, T., Spence, G. D., Riedel, M., Hyndman, R. D., & Chapman, N. R. (2007). Fluid flow and origin of a carbonate mound offshore Vancouver island: Seismic and heat flow constraints. *Marine Geology*, *239*(1–2), 83–98. https://doi.org/10.1016/j.margeo.2007.01.002

Hensen, C., Nuzzo, M., Hornibrook, E., Pinheiro, L. M., Bock, B., Magalhães, V. H., & Brückmann, W. (2007). Sources of mud volcano fluids in the Gulf of Cadiz - indications for hydrothermal imprint. *Geochimica et Cosmochimica Acta*, *71*, 1232–1248. https://doi.org/10.1016/j.gca.2006.11.022

Hensen, C., Scholz, F., Nuzzo, M., Valadares, V., Gràcia, E., Terrinha, P., et al. (2015). Strike-slip faults mediate the rise of crustal-derived fluids and mud volcanism in the deep sea. *Geology*, *43*(4), 339–342. https://doi.org/10.1130/G36359.1

Hoehler, T. M., Alperin, M. J., Albert, D. B., & Martens, C. S. (1994). Field and laboratory studies of methane oxidation in an anoxic marine sediment—Evidence for a methanogen sulfate reducer consortium. *Global Biogeochemical Cycles*, *8*(4), 451–463. https://doi.org/10.1029/94GB01800

Hutchinson, J. A., Kao, H., Spence, G., Obana, K., Wang, K., & Kodaira, S. (2019). Seismic characteristics of the Nootka fault zone: Results from the Seafloor Earthquake Array Japan-Canada Cascadia Experiment (SeaJade). *Bulletin of the Seismological Society of America*, *109*(6), 2252–2276. https://doi.org/10.1785/0120190008

Hyndman, R. D., & Davis, E. E. (1992). A mechanism for the formation of methane hydrate and seafloor bottom-simulating reflectors by vertical fluid expulsion. *Journal of Geophysical Research*, *97*(B5), 7025–7041. https://doi.org/10.1029/91JB03061

Hyndman, R. D., Riddihough, R. P., & Herzer, R. (1979). The Nootka fault zone—A new plate boundary off western Canada. *Geophysical Journal International*, *58*(3), 667–683. https://doi.org/10.1111/j.1365-246X.1979.tb04801.x

Hyndman, R. D., Wang, K., Yuan, T., & Spence, G. D. (1993). Tectonic sediment thickening, fluid expulsion, and the thermal regime of subduction zone accretionary prisms: The Cascadia margin off Vancouver Island. *Journal of Geophysical Research*, *98*(B12), 21,865–21,876. https://doi.org/10.1029/93JB02391

Hyndman, R. D., & Weichert, D. H. (1983). Seismicity and rates of relative motion on the plate boundaries of Western North America. *Geophysical Journal of the Royal Astronomical Society*, *72*(1), 59–82. https://doi.org/10.1111/j.1365-246X.1983.tb02804.x

Johnson, J. E., Mienert, J., Plaza-Faverola, A., Vadakkepuliyambatta, S., Knies, J., Bünz, S., et al. (2015). Abiotic methane from ultraslow-spreading ridges can charge Arctic gas hydrates. *Geology*, *43*(5), 371–374. https://doi.org/10.1130/G36440.1

Kluesner, J. W., & Brothers, D. S. (2016). Seismic attribute detection of faults and fluid pathways within an active strike-slip shear zone: New insights from high-resolution 3D P-Cable seismic data along the Hosgri Fault, offshore California. *Interpretation*, *4*(1), SB131–SB148. https://doi.org/10.1190/INT-2015-0143.1

Kreemer, C., Govers, R., Furlong, K. P., & Holt, W. E. (1998). Plate boundary deformation between the Pacific and North America in the Explorer region. *Tectonophysics*, *293*, 225–238. https://doi.org/10.1016/S0040-1951(98)00089-4

Kuna, V. M., Nábělek, J. L., & Braunmiller, J. (2019). Mode of slip and crust-mantle interaction at oceanic transform faults. *Nature Geoscience*, *12*(2), 138–142. https://doi.org/10.1038/s41561-018-0287-1

Labonte, A. L. (2007). *An investigation of deformation and fluid flow at subduction zones using newly developed instrumentation and finite element modeling* (PhD dissertation). San Diego, CA: University of California.

Lapham, L. L., Chanton, J. P., Martens, C. S., Sleeper, K., & Woolsey, J. R. (2008). Microbial activity in surficial sediments overlying acoustic wipe-out zones at a Gulf of Mexico cold seep. *Geochemistry, Geophysics, Geosystems*, *9*, Q06001. https://doi.org/10.1029/02008GC001944

Loher, M., Pape, T., Marcon, Y., Römer, M., Wintersteller, P., Praeg, D., et al. (2018). Mud extrusion and ring-fault gas seepage—Upward branching fluid discharge at a deep-sea mud volcano. *Scientific Reports*, *8*, 6275. https://doi.org/10.1038/s41598-018-24689-1

Magen, C., Lapham, L. L., Pohlman, J. W., Marshall, K., Bossman, S., & Chanton, J. P. (2014). A simple headspace equilibration method for measuring dissolved methane. *Limnology and Oceanography: Methods*, *12*, 637–650 https://doi.org/10.4319/lom.2014.12.637

Mayer, L. A. (2001). *Performance and progress report: UNH/NOAA Joint Hydrographic Center, NOAA Ref. No.: NA970G0241,* (pp. 1-35). Available at http://ccom.unh.edu/sites/default/files/progress_reports/Report_12-31_2001.pdf [last visited April 25, 2019]

McClymont, A. F., & Clowes, R. M. (2005). Anomalous lithospheric structure of Northern Juan de Fuca plate—A consequence of oceanic rift propagation? *Tectonophysics*, *406*, 231–231. https://doi.org/10.1016/j.tecto.2005.05.026

McDermott, J. M., Seewald, J. S., German, C. R., & Sylva, S. P. (2015). Pathways for abiotic organic synthesis at submarine hydrothermal fields. *Proceedings of the National Academy of Science of the United States of America*, *112*(25), 7668–7672. https://doi.org/10.1073/pnas.1506295112

McGuire, J. J. (2019). The geology of earthquake swarms. *Nature Geoscince*, *12*(2), 82–83. https://doi.org/10.1038/s41561-019-0302-1

McGuire, J. J., Collins, J. A., Gouédard, P., Roland, E., Lizarralde, D., Boettcher, M. S., et al. (2012). Variations in earthquake rupture properties along the Gofar transform fault, East Pacific Rise. *Nature Geoscience*, *5*(5), 336–341. https://doi.org/10.1038/ngeo1454

Milkov, A. V., & Etiope, G. (2018). Revised genetic diagrams for natural gases based on a global dataset of >20,000 samples. *Organic Geochemsitry*, *125*, 109–120. https://doi.org/10.1016/j.orggeochem.2018.09.002

Obana, K., Scherwath, M., Yamamoto, Y., Kodaira, S., Wang, K., Spence, G., et al. (2015). Earthquake activity on northern Cascadia subduction zone off Vancouver Island revealed by Ocean Bottom Seismograph observations. *Bulletin of the Seismological Society of America*, *105*(1), 489–495. https://doi.org/10.1785/0120140095

Paull, C. K., Dallimore, S. R., Caress, D. W., Gwiazda, R., Melling, H., Riedel, M., et al. (2015). Active mud volcanoes on the continental slope of the Canadian Beaufort Sea. *Geochemistry, Geophysics, Geosystems*, *16*, 3160–3181. https://doi.org/10.1002/2015GC005928

Paull, C. K., Normark, W. R., Ussler, W. III, Caress, D. W., & Keaten, R. (2008). Association among active seafloor deformation, mound formation, and gas hydrate growth and accumulation within the seafloor of the Santa Monica Basin, offshore California. *Marine Geology*, *250*(3-4), 258–275. https://doi.org/10.1016/j.margeo.2008.01.011

Perez-Garcia, C., Berndt, C., Klaeschen, D., Mienert, J., Haffert, L., Depreiter, D., & Haeckel, M. (2011). Linked halokinesis and mud volcanism at the Mercator mud volcano, Gulf of Cadiz. *Journal of Geophysical Research*, *116*, B05101. https://doi.org/10.1029/2010JB008061

Pockalny, R. A., Fox, P. J., Fornari, D. J., Macdonald, K. C., & Perfit, M. R. (1997). Tectonic reconstruction of the Clipperton and Siqueiros fracture zones: Evidence and consequences of plate motion change for the last 3 Myr. *Journal of Geophysical Research*, *102*, 3167–3181. https://doi.org/10.1029/96JB03391

Pohlman, J. W., Bauer, J. E., Canuel, E. A., Grabowski, K. S., Knies, D. L., Mitchell, C. S., et al. (2009). Methane sources in gas hydrate-bearing cold seeps: Evidence from radiocarbon and stable isotopes. *Marine Chemistry*, *115*, 102–109. https://doi.org/10.1016/j.marchem.2009.07.001

Pohlman, J. W., Canuel, E. A., Chapman, N. R., Spence, G. D., Whiticar, M. J., & Coffin, R. B. (2005). The origin of thermogenic gas hydrates on the northern Cascadia Margin as inferred from isotopic (13C/12C and D/H) and molecular composition of hydrate and vent gas. *Organic Geochemistry*, *36*(5), 703–716. https://doi.org/10.1016/j.orggeochem.2005.01.011

Pohlman, J. W., Kaneko, M., Heuer, V. B., Coffin, R. B., & Whiticar, M. (2009). Methane sources and production in the northern Cascadia margin gas hydrate system. *Earth and Planetary Science Letters*, *287*(3–4), 504–512. https://doi.org/10.1016/j.epsl.2009.08.037

Pohlman, J. W., Riedel, M., Bauer, J. E., Canuel, E. A., Paull, C. K., Lapham, L., et al. (2013). Anaerobic methane oxidation in low-organic content methane seep sediments. *Geochimica et Cosmochimica Acta*, *108*, 184–201. https://doi.org/10.1016/j.gca.2013.01.022

Praeg, D., Ceramicola, S., Barbieri, R., Unnithan, V., & Wardell, N. (2009). Tectonically-driven mud volcanism since the late Pliocene on the Calabrian accretionary prism, central Mediterranean Sea. *Journal of Marine and Petroleum Geology*, *26*(9), 1849–1865. https://doi.org/10.1016/j.marpetgeo.2009.03.008

Prigent, C., Warren, J. M., Kohli, A. H., & Teyssier, C. (2020). Fracture-mediated deep seawater flow and mantle hydration on oceanic transform faults. *Earth and Planetary Science Letters*, *532*, 115988. https://doi.org/10.1016/j.epsl.2019.115988

Riddihough, R. (1984). Recent movements of the Juan de Fuca plate system. *Journal of Geophysical Research*, *89*(B8), 6980–6994. https://doi.org/10.1029/JB089iB08p06980

Riedel, M., Collett, T. S., & Malone, M. (2010). Expedition 311 synthesis: Scientific findings. In M. Riedel, T. S. Collett, M. J. Malone, & Expedition 311 Scientists (Eds.), *Proceeding of the International Ocean Discovery Program* (Vol. 311, pp. 1–28). Washington, DC: Integrated Ocean Drilling Program Management International, Inc. https://doi.org/10.2204/iodp.proc.311.213.2010

Riedel, M., Conway, K. W., Côté, M. M., Middleton, G., Neelands, P. J., Obana, K., et al. (2014). *Report of Cruise 2014006PGC, SeaJade-II Seafloor Earthquake Array Japan-Canada Cascadia Experiment, OBS recovery* (Open File 7715, pp. 1-27). Geological Survey of Canada. https://doi.org/10.4095/295548

Riedel, M., Côté, M. M., Manning, D., Middleton, G., Murphy, R., Neelands, P. J., et al. (2014). *Report of Cruise 2013008PGC, SeaJade-II Seafloor Earthquake Array Japan-Canada Cascadia Experiment, OBS deployment and piston coring of slope failures* (Open File 7716, pp. 1-64). Geological Survey of Canada. https://doi.org/10.4095/295552

Riedel, M., Côté, M. M., Neelands, P. J., Obana, K., Wania, R., Price, A., & Taylor, S. (2014). *Report of Cruise 2010007PGC, C.C.G. Vessel John P. Tully, 30 June–10 July 2010, SeaJade-I Seafloor Earthquake Array-Japan Canada Cascadia Experiment, Ocean bottom seismometer recovery, methane gas-plume acoustic imaging, and CTD-water sampling program* (Open File 7557, pp. 1-85). Geological Survey of Canada. https://doi.org/10.4095/295545

Riedel, M., Côté, M. M., Urlaub, M., Geersen, J., Scholz, N., Naegeli, K., & Spence, G. D. (2018). Slope failures along the deformation front of the Cascadia margin: Linking slide morphology to subduction-zone parameters. *Geological Society, London, Special Publications*, *477*(1), 47–67. https://doi.org/10.1144/SP477.33

Riedel, M., Kelly, D. S., Delaney, J. R., Spence, G. D., Hyndman, R. D., Mayer, L., et al. (2001). *Discovery of an active submarine mud volcano along the Nootka Fault West of Vancouver Island*. Paper presented at American Geophysical Union Fall Meeting 2001.

Riedel, M., Tréhu, A. M., & Spence, G. D. (2010). Characterizing the thermal regime of cold vents at the northern Cascadia margin from bottom-simulating reflector distributions, heat-probe measurements and borehole temperature data. *Marine Geophysical Researches*, *31*, 1. https://doi.org/10.1007/s11001-010-9080-2

Ristau, J., Rogers, G. C., & Cassidy, J. F. (2006). Stress in western Canada from regional moment tensor analysis. *Canadian Journal of Earth Sciences*, *44*, 127–148.

Ristau, J.P. (2004). *Seismotectonics of Western Canada from regional moment tensor analysis* (PhD thesis). British Columbia, Canada: University of Victoria.

Rohr, K. M. M., Furlong, K., & Riedel, M. (2018). Initiation of strike-slip faults, serpentinization and methane: The Nootka fault zone, the Juan de Fuca-Explorer plate boundary. *Geochemistry, Geophysics, Geosystems*, *19*, 4290–4312. https://doi.org/10.1029/2018GC007851

Rohr, K. M. M., & Furlong, K. P. (1996). Images of the initiation of a transform plate boundary, the Explorer transform zone. *Eos, Transactions American Geophysical Union*, *77*, F655.

Rohr, K. M. M., & Gröschel-Becker, H. (1994). Correlation of well logs, physical properties, and surface seismic reflection data, Middle Valley, Juan de Fuca Ridge. In M. J. Mottl, E. E. Davis, A. T. Fisher, & J. F. Slack (Eds.), *Proceedings of the Ocean Drilling Program, Sciencetific Results* (Vol. 139, pp. 585–596). College Station, TX: Ocean Drilling Program. https://doi.org/10.2973/odp.proc.sr.139.257.1994

Rohr, K. M. M., & Schmidt, U. (1994). Seismic structure of Middle Valley near Sites 855–858, Leg 139, Juan de Fuca Ridge. In M. J. Mottl, E. E. Davis, A. T. Fisher, & J. F. Slack (Eds.), *Proceedings of the Ocean Drilling Program, Sciennetific Results* (Vol. 139, pp. 3–17). College Station, TX: Ocean Drilling Program. https://doi.org/10.2973/odp.proc.sr.139.204.1994

Rohr, K. M. M., & Tyron, A. J. (2010). Pacific-North America Plate boundary reorganization in response to a change in relative plate motion: Offshore Canada. *Geochemistry, Geophysics, Geosystems*, *11*, Q06007. https://doi.org/10.1029/2009GC003019

Roland, E., Lizarralde, D., McGuire, J. J., & Collins, J. A. (2012). Seismic velocity constraints on the material properties that control earthquake behavior at the Quebrada-Discovery-Gofar transform faults, East Pacific Rise. *Journal of Geophysical Research*, *117*, B11102. https://doi.org/10.1029/2012JB009422

Ryan, W. B. F., Carbotte, S. M., Coplan, J. O., O'Hara, S., Melkonian, A., Arko, R., et al. (2009). Global multi-resolution topography synthesis. *Geochemistry, Geophysics, Geosystems*, *10*, Q03014. https://doi.org/10.1029/2008GC002332

Scherwath, M., Spence, G. D., Obana, K., Kodaira, S., Wang, K., Riedel, M., et al. (2011). Seafloor seismometers monitor northern Cascadia earthquakes. *Eos, Transactions American Geophysical Union*, *92*(47), 421–422. https://doi.org/10.1029/2011EO470001

Schreier, J. E., & Lutz, R. A. (2019). Hydrothermal vent biota. *Encyclopedia of ocean sciences* (3rd ed., Vol. 4, pp. 308–319). London, UK: Academic Press. https://doi.org/10.1016/B978-0-12-409548-9.11391-0

Scribano, V., Carbone, S., Manuella, F. C., Hovland, M., Rueslatten, H., & Johnsen, H. K. (2017). Origin of salt giants in abyssal sepentinite systems. *International Journal of Earth Sciences*, *106*(7), 2595–2608. https://doi.org/10.1007/s00531-017-1448-y

Spence, G. D., Coffin, R., & Hoehnle, J. (2001). *VENTFLUX 2: Single channel seismics, piston coring and CTD casts associated with gas hydrates offshore Vancouver Island, Report of Cruise PGC01-003 C.C.G. Vessel John P. Tully 23 July – 12 August 2001* (pp. 1-130). University of Victoria.

Spence, G. D., & Riedel, M. (2014). *Report of Cruise 2010005PGC, C.C.G. Vessel John P. Tully, 22 September – 2 October 2010, SeaJade-I Seafloor Earthquake Array Japan-Canada Cascadia Experiment, Ocean bottom seismometer deployment and active-source airgun refraction and reflection program* (Open File 7758, pp. 1-50). Geological Survey of Canada. https://doi.org/10.4095/295546

Spence, G. D., & Willoughby, E. C. (2004). *SEICOMAG: Single-Channel Seismic, Compliance and Electromagnetic Measurements Offshore Vancouver Island, Report of Cruise PGC04-08 C.C.G. Vessel John P. Tully 22 July – 10 August 2004* (pp. 1-89). University of Victoria.

Tréhu, A. M., Stakes, D. S., Bartlett, C. D., Chevallier, J., Duncan, R. A., Goffredi, S. K., et al. (2003). Seismic and seafloor evidence for free gas, gas hydrates, and fluid seeps on the transform margin offshore Cape Mendocino. *Journal of Geophysical Research*, *108*(B5), 2263. https://doi.org/10.1029/2001JB001679

Underwood, M. B., Hoke, K. D., Fisher, A. T., Davis, E. E., Giambalvo, E., Zühlsdorff, L., & Spinelli, G. A. (2005). Provenance, stratigraphic architecture, and hydrogeologic influence of turbidites on the mid-ocean ridge flank of northwestern Cascadia Basin, Pacific Ocean. *Journal of Sedimentary Research*, *75*, 149–164. https://doi.org/10.2110/jsr.2005.012

Whiticar, M. J. (1999). Carbon and hydrogen isotope systematics of bacterial formation and oxidation of methane. *Chemical Geology*, *161*(1-3), 291–314. https://doi.org/10.1016/S0009-2541(99)00092-3

Wilcock, W. S. D., McGill, P. R., Hooft, E. E. E., Toomey, D. R., Patel, H. M., Stakes, D. S., et al. (2007). *The deployment of a long-term seismic network on the Juan de Fuca Ridge*. Paper presented at the Oceans 2007 Meeting, Vancouver.

Willoughby, E. C., & Fyke, J. (2003). *BofFiNS 2003: Gas hydrate investigation at bullseye and fish-boat and survey of the intersection of the Nootka Fault with the continental margin using single-channel seismic streamer, Cruise PGC03-004: 3 August- 29 August, 2003 C.C.G.S. John P. Tully, CEOR Report 2003-8* (1-50). University of Victoria.

Willoughby, E. C., & Hyndman, R. D. (2005). Earthquake rate, slip rate, and the effective seismic thickness for oceanic transform faults of the Juan de Fuca plate system. *Geophysical Journal International*, *160*(3), 855–868. https://doi.org/10.1111/j.1365-246X.2005.02523.x

Yoshinaga, M. Y., Holler, T., Goldhammer, T., Wegener, G., Pohlman, J. W., Brunner, B., et al. (2014). Carbon isotope equilibration during sulphate-limited anaerobic oxidation of methane. *Nature Geoscience*, *7*(3), 190–194. https://doi.org/10.1038/ngeo2069